LONG-TERM EVOLUTION OF SOLAR CORONAL HOLES

AMR HAMADA

University of Oulu Graduate School

Space Physics and Astronomy Research Unit

Faculty of Science

University of Oulu

Finland

Academic Dissertation to be presented, with the assent of the Graduate School of the University of Oulu, for public discussion in the Auditorium IT115, Linnanmaa, on November 6th, 2020, at 12 o'clock noon.

REPORT SERIES IN PHYSICAL SCIENCES Report no. 137

OULU 2020 • UNIVERSITY OF OULU

Opponent

Prof. Minna Palmroth, University of Helsinki, Finland

Custos

Prof. Kalevi Mursula, University of Oulu, Finland

Pre-examiners

Prof. Dean Pesnell, Project Scientist for the Solar Dynamics Observatory, NASA, USA

Prof. Periasamy Manoharan, Senior Observatory Scientist, Arecibo Observatory: Arecibo, Puerto Rico, USA

Supervisors

Prof. Kalevi Mursula, University of Oulu, Finland

Doc. Timo Asikainen, University of Oulu, Finland

ISBN 978-952-62-2753-5

ISBN 978-952-62-2754-2 (PDF)

ISSN 1239-4327

Punamusta Oy 2020

Hamada, Amr,

Long-term evolution of solar coronal holes
Space Physics and Astronomy Research Unit, University of Oulu, Finland
Report No. 137 (2020)

Abstract

Solar coronal holes are regions of open magnetic field lines in the solar corona. They are the source region of high-speed solar wind streams that play an important role for geomagnetic activity and are the most important driver of energetic particle precipitation into the Earth's atmosphere. Understanding the evolution of coronal holes is critical for solar magnetism as well as for accurate space weather forecasts. Historically, coronal holes have been identified visually and hand-traced by experienced observers. In this thesis, we develop a novel automated method to identify coronal holes from the extreme ultraviolet synoptic maps by determining the intensity threshold of coronal hole regions separately for each synoptic map. We quantify the spatio-temporal evolution of coronal hole during solar cycles 23 and 24. We studied geomagnetic storms triggered by two sequences of high-speed streams from persistent low-latitude coronal hole sources, observed in the declining phase of solar cycle 23. We found a systematic change in the Bz(GSM)–Bz(GSE) difference which offers the first detailed analysis of the onset of the Rusell-McPherron mechanism, increasing geomagnetic activity of the negative-polarity sequence as we approach the March equinox. We also present a novel homogenized solar extreme ultraviolet synoptic dataset based on full-disk images from Solar and Heliospheric Observatory/Extreme ultraviolet Imaging Telescope and Solar Dynamics Observatory/Atmospheric Imaging Assembly. These maps provide a systematic and homogenous view of the entire solar surface in the extreme ultraviolet wavelengths from 1996 until 2019. Using this long-running homogenized dataset of solar extreme ultraviolet observations together with the coronal hole automated identification algorithm, we prepared a 23-year (1996–2019) coronal hole synoptic dataset. This coronal hole dataset is combined with the MacIntosh Archive (1973–2009) to produce the longest dataset of equatorial coronal hols covering more than four solar cycles.

Keywords: Coronal holes, geomagnetic activity, high-speed streams, computer vision, automated algorithm, synoptic maps, High speed stream

"*Preserving knowledge is easy. Transferring knowledge is also easy. But making new knowledge is neither easy nor profitable in the short term. Fundamental research proves profitable in the long run, and, as importantly, it is a force that enriches the culture of any society with reason and basic truth.*"

– Ahmed Zewail,
Winner of the Nobel Prize (1999)

إِلَيّ رَوْحٌ أَعَزّ الرِّجَال ، أَبِي

وَإِلَى أُمِّي الْغَالِيَة ، حَفِظَهَا اللَّهُ

Preface

This work has been carried out in the Space Physics and Astronomy Research Unit of the University of Oulu. First, I want to express my gratitude to Prof. Kalevi Mursula, who demonstrated me the necessary amount of diligence needed for finding new things out. I also want to thank my second supervisor, Dr. Timo Asikainen, for many useful discussions and debates.

I would like to express my sincerest appreciation to all the members of the Space Physics and Astronomy Research Unit and my follow-up group members, Prof. Jürgen Schmidt, Prof. Ilya Usoskin and Prof. Esa Turunen. Directly or indirectly you all have contributed to the work that is presented here.

A further special thanks to my wife Dina, who took all the extra loads during my absence from home, for her unreserved support and unspeakable patience she showed throughout this work. Without her kind support and encouragement this work would not have been organized like this. I am deeply, and still, joyful to my lovely kids HaBiBah and MoHaMed, and those who may come in the future:P, for filling our life with a lot of action and happiness.

Thank you my brothers, Alaaeldin and Ahmed, for always having my back. We have made many memories throughout our lives, and there will be many more to make in the future isa.

Last, certainly not least, I need to thank my parents Mohamed and Eman. My mind fails to find words that can show how deeply I am indebted and grateful to you for your unconditional love and care. You have always been, and still, supportive and encouraging to me. My warm regards.

Oulu, June 29, 2020

Amr Hamada

Original publications

This thesis consists of an introduction and four original papers.

I *Hamada, A., Asikainen, T., Virtanen, I. and Mursula,K., Automated Identification of Coronal Holes from Synoptic EUV Maps, Sol. Phys. (2018) 293: 71.*

II *Munteanu, C., Hamada, A., Mursula, K., High-speed solar wind streams in 2007-2008: Turning on the Russell-McPherron effect. Journal of Geophysical Research: Space Physics (2019), 124.*

III *Hamada, A., Asikainen, T., Mursula, K., New Homogeneous Dataset of Solar EUV synoptic maps from SOHO/EIT and SDO/AIA. Sol. Phys. (2019) 295, 2.*

IV *Hamada, A., Asikainen, T., and Mursula,K., A uniform series of coronal holes in 1973-2018, Sol. Phys. (2020). (Submitted)*

In the text, original papers are referred to using Roman numerals I–V.

The author performed the data analysis and was also the responsible writer in Papers I, III and IV. In paper II the author contributed to the coronal hole data analysis and interpretation.

Contents

1. Introduction

The Sun and especially its outer layer, the corona, are the topic of this thesis. The Sun is nearly a perfect sphere of hot plasma that holds 99.8 percent of the solar system's mass and its diameter is roughly 109 times the diameter of the Earth. The convective motions of plasma inside the Sun generate the solar magnetic field via a dynamo process. The Sun was formed about 4.6 billion years ago and has enough nuclear fuel to stay much as it is now for another 5 billion years. The Sun is divided into several layers. The solar interior, from the inside to out, is made up of the core, the radiative zone and the convective zone. The solar atmosphere consists of the photosphere, the chromosphere, the transition region and the outer layer, corona.

Corona expands into interplanetary space as a flow of plasma called the solar wind, which also carries with it the solar magnetic field. The region of space dominated by the solar wind and the embedded solar magnetic field is called the heliosphere. The magnetic field of the solar wind is often called the interplanetary magnetic field (IMF) or the heliospheric magnetic field (HMF). One of the most important features of the solar wind are the high-speed streams (HSSs), which are the dominant driver of energetic particle precipitation into the Earth's atmosphere [e.g., *Asikainen and Ruopsa*, 2016] and also give rise to recurrent geomagnetic activity [*Mursula et al.*, 2015]. At high latitudes, most of the aurora are produced by HSSs when the upper atmosphere becomes excited by precipitating energetic particles.

HSSs are known to originate from solar coronal holes (CHs), which are coronal regions characterized by lower electron density than the typical background corona. This is because CHs have open magnetic fields with one predominant magnetic polarity [*Wang*, 2004]. The earliest EUV observations of coronal holes were made by *Tousey et al.* [1968], who noted from spectroheliograms obtained by rocket experiments that EUV emission in polar regions of the Sun seemed to be weaker than in the surrounding regions. In the 1970s, CHs were observed as discrete dark patches in X-ray and EUV solar disk images [*Krieger et al.*, 1973; *Zirker*, 1977].

It is difficult to uniquely and objectively identify coronal holes on solar images. They appear differently in different wavelengths, which makes it somewhat arbitrary to use observations of one wavelength only to determine their characteristics. The area, shape, and darkness of any given hole are not the same in different observing wavelengths [*Kahler et al.*, 1983; *Harvey and Recely*, 2002]. The CH boundary is not sharp and is often partly obscured by magnetic structures related to surrounding active regions. Coronal holes, both polar and equatorial, have historically been identified visually and hand-traced by experienced observers. However, different human observers typically determine the CH boundaries differently. Moreover, manual detection methods are extremely time-consuming and problematic in quantitative studies.

A new dynamical and adaptive CH detection algorithm is presented in this thesis. The algorithm is designed to be as robust as possible against temporal changes in EUV intensity. We compare and use the information contained in observations made at different wavelengths. We also present a new homogenized EUV synoptic dataset and study the properties of the solar coronal holes and high-speed streams, their spatio-temporal evolution and interaction with the magnetosphere.

2. Solar structure

2.1. Solar interior

The Sun's interior can be divided into three different zones based on their poroperties [*Phillips*, 1992]: *core*, *radiative zone* and *convective zone* (see Figure 2.1). In the core, temperature is about 1.5×10^7K. The huge pressure due to gravitational self-attraction condenses solar matter, providing the conditions for nuclear fusion, the energy source of the Sun. The core extends to about 0.25 R_s (R_s is the solar radius). The radiative zone forms between 0.25 - 0.7 R_s where the energy is transported by collision of photons with matter particles. The temperature gradient is small enough to keep the matter stably stratified. With increasing radial distance, the density drops and the matter becomes cooler. The formation of atoms makes the matter opaque to radiative and the solar plasma hydrostatically unstable [*Phillips*, 1992]. Therefore, the energy in the radiative zone is transferred by thermal convection. Convective instability allows the plasma to rise and fall in a cellular circulation, creating structures known as supergranular and granular cells [*Rieutord and Rincon*, 2010]. The latter can also be observed on the visible solar surface.

While the radiative zone and core rotate as a rigid body, the convective zone rotates differentially, creating a region between the radiative and convective zone that has a very large shear in rotation rate (see Figure 2.2). This region is named the tachocline. Above, the convective zone exhibits differential rotation varying with latitude [*Howe*, 2009]. A dynamo mechanism operating in the tachocline is generally considered to be the source of the Sun's magnetic field [*Charbonneau*, 2010].

2.2. Solar atmosphere

Figure 2.3 shows the density and temperature profiles above the photosphere, the visible surface of the Sun, as a function of altitude. Based on the temperature

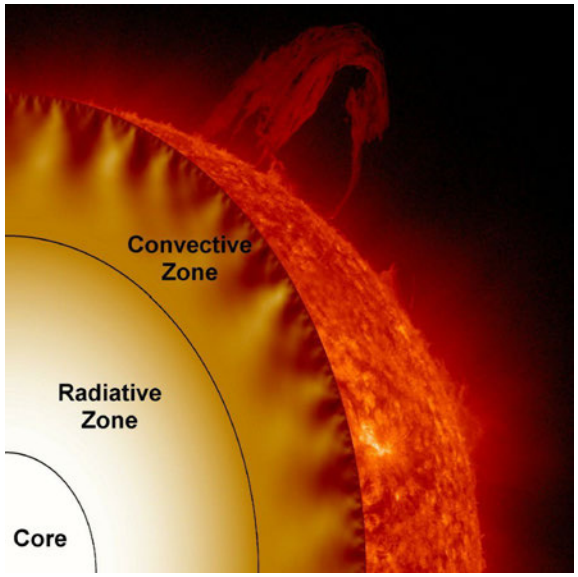

Fig. 2.1. Schematic view of the Sun's structure from its interior to the atmosphere. Image credit: NASA.

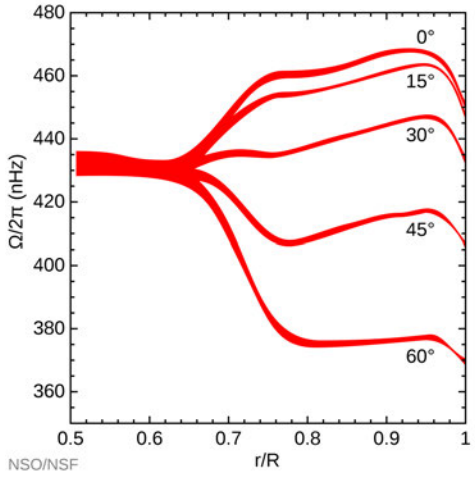

Fig. 2.2. Internal rotation in the Sun, showing differential rotation in the convective zone and almost uniform rotation in the radiative zone. The transition between these zones is called the tachocline. Image credit: NSO/GONG.

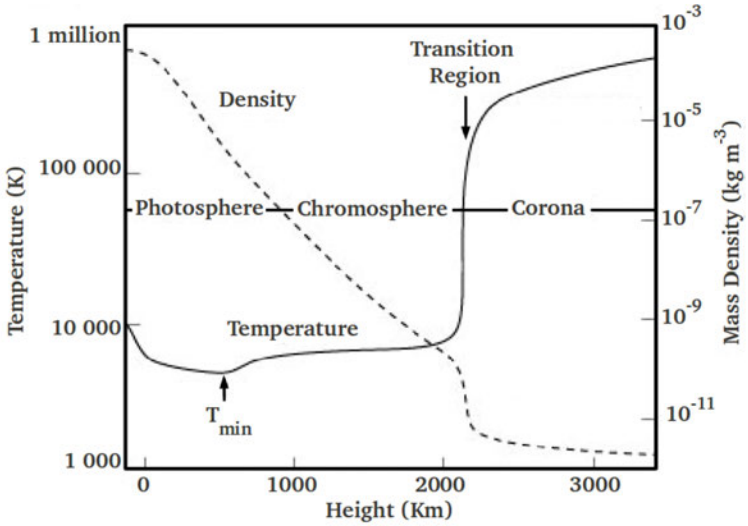

Fig. 2.3. A model of the altitude profile of temperature and density in the solar atmosphere. Zero corresponds to the solar surface, based on the optical depth [*Lang*, 2001].

profile, the solar atmosphere is divided into the photosphere, the chromosphere, the transition region and the corona. They are not static, well separated layers but structured and temporally evolving regions, unlike the lower layers of the Sun where gravity dominates.

Photosphere is a layer where a transition from the hydrostatically unstable convective zone to a hydrostatically stable atmosphere takes place. It is a thin layer (400–500 km altitude) where the atmosphere becomes sufficiently transparent so that the photons can escape from the Sun. Majority of solar radiation emitted into interplanetary space comes directly from this layer. Because of this, the gas becomes cooler and its temperature reaches a minimum of about 4500 K at the top of the photosphere.

Chromosphere is a fairly narrow layer above the photosphere (at about 500 - 2500 km altitude) where temperature increases again with height. In the chromosphere, the plasma is still partially ionised. Pressure balance in the presence of a steep increase of temperature requires a steep decrease in density (see Figure 2.3). Organized magnetic field structures can be observed in the chromosphere because the plasma pressure is not sufficient to control the magnetic fields as in the photosphere.

In the transition region between the chromosphere and the corona the tempera-

ture rapidly increases from 10^4 K to about several 10^6 K [*Lang*, 2001] and plasma becomes fully ionised. Detailed physical properties of this layer still remain unclear.

Corona is the outer atmosphere of the Sun with a high temperature of several 10^6 K and an extremely low density (about 0.3×10^{-11} kg m^{-3}). The existence of a hot solar corona is still puzzling. Several theories have been proposed for coronal heating, the two most popular candidates being the wave theory [*Narain and Ulmschneider*, 1996] and the microflare/nanoflare theory based on magnetic reconnection [*Podladchikova et al.*, 2002; *Klimchuk*, 2017].

2.3. Sunspots and solar cycle

Sunspots are dark regions on the solar surface (Figure 2.4) with strong magnetic field concentrations welling up to the photosphere, often surrounded by large active regions. In the sunspot dark center, umbra, the magnetic field strength is large, typically 4000 G [*Okamoto and Sakurai*, 2018; *Livingston et al.*, 2006], much larger than the average magnetic field of the solar surface, which is about 10 G. Due to the strong magnetic field of the umbra, the convective heat transport is inhibited, which makes this area cooler and darker in the continuum spectrum than the surrounding surface. Around the umbra, a penumbra is often formed which has a lower magnetic field strength (around 2000 G) and a filament structure. A typical lifetime of sunspots is only a couple of days, but they can persist for weeks or even months before dissipating.

The position and the number of sunspots also change in time (Figure 2.5). In the early phase of the solar cycle they appear between the latitudes of 30° and 40°. As the cycle progresses, sunspot occurrence moves towards the solar equator. By plotting the latitudinal position of the sunspots versus time we obtain the so called butterfly diagram (Figure 2.5). This diagram shows the spatial and temporal distribution of sunspots.

Sunspots have been directly observed for more than 400 years since the first telescope observation. *Schwabe* [1844] was the first who discovered the roughly 11-year periodicity in the number of sunspots. Conventionally, the sunspot cycle that began in 1755 is referred to as cycle 1. *Hale* [1908] discovered the existence of a strong magnetic field in sunspots. At solar cycle (SC) maximum times, the many sunspots make the solar magnetic field stronger and quite complex. At solar maximum times, the solar magnetic field is stronger and produces also many sunspot.

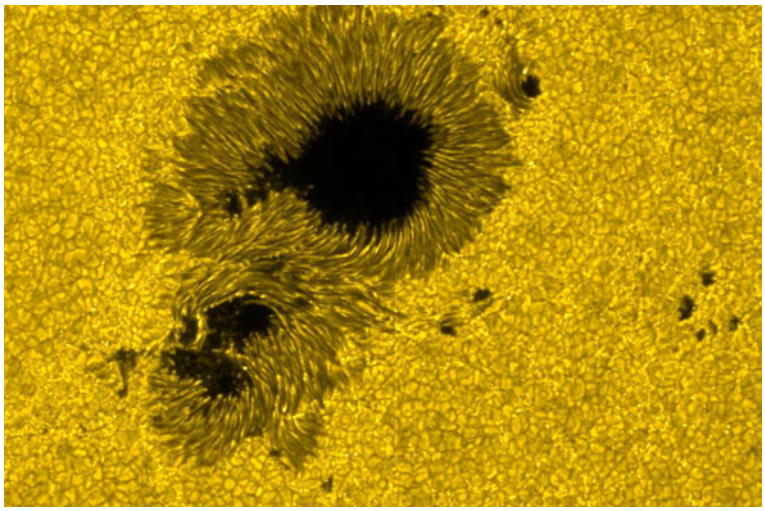

Fig. 2.4. Sunspot group of the active region 10930 (size around 20000 km). Dark areas are the sunspot umbrae, surrounded by the less dark penumbra. Regular granular structure (yellow) is seen outside the sunspot group. Image taken by Hinode's Solar Optical Telescope (SOT) on 13 December 2006.

2.4. Solar magnetic cycle

Solar magnetic fields are produced in the convective zone by electric currents which are generated by the flow of the Sun's hot, ionized gas. At the minimum phase of the solar cycle, the large-scale solar magnetic field is dipole-like (see Figure 2.6). Unipolar magnetic fields are then concentrated in the polar region with a mean field of several gauss [*Svalgaard et al.*, 1978; *Tsuneta et al.*, 2008]. Around the next solar maximum phase, decaying active-region flux migrates poleward making the polar field and the dipole moment reverse sign [*Babcock*, 1959]. This poleward migration of the magnetic field is due to meridional circulation of the plasma on the solar surface [*Babcock*, 1961; *Leighton*, 1969]. The solar magnetic cycle takes a period of 22 years.

One concept which is considered to drive the solar cycle is the so called α - Ω dynamo combined with the meridional circulation of the convective zone [*Dikpati and Gilman*, 2009]. Assuming the poloidal field as an initial seed magnetic field, the Ω effect consists of a wrapping of the poloidal magnetic field by differential rotation (Figure 2.7 a). As a result, the field develops strong toroidal flux tubes (Figure 2.7 b). The toroidal field is transported to the surface of the Sun by buoyancy. During the transport through the convective zone the toroidal field develops a kink due to the Coriolis force (α effect; Figure 2.7 c, d). Meridional flow (Figure 2.7 g)

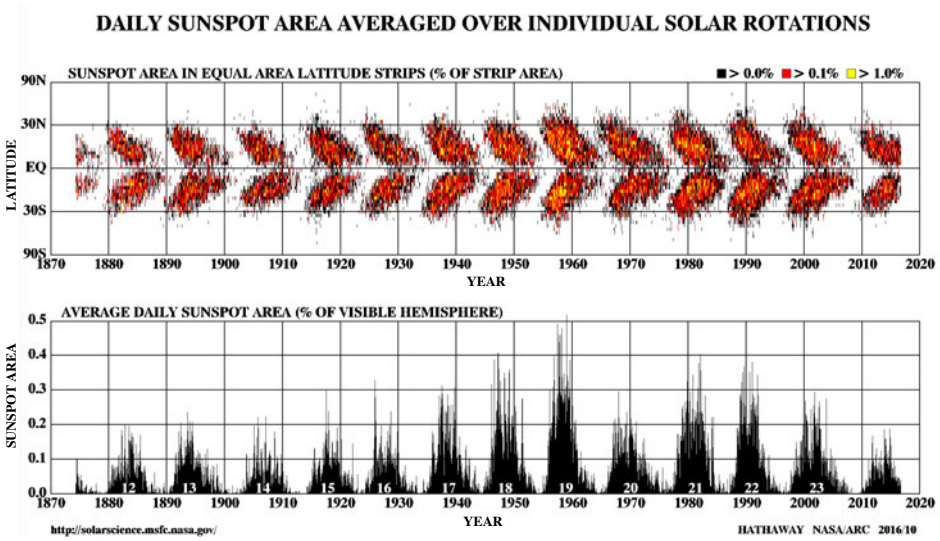

Fig. 2.5. Temporal evolution of sunspot area. The upper panel shows the latitudinal distribution of sunspot over time (butterfly diagram). The lower panel shows the average daily sunspot area over time (Image credit: http://solarcyclescience.com/solarcycle.html).

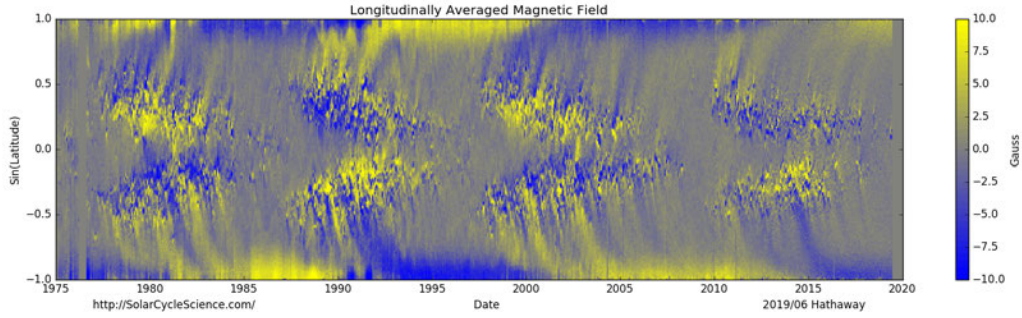

Fig. 2.6. Distribution of the (longitudinally averaged) surface magnetic field over the last four solar cycles. Yellow regions are occupied by away-pointing (positive) magnetic fields and blue denotes toward-pointing (negative) fields. Poles have opposite polarities that switch from one cycle to the next near the time of solar maximum (Image credit: http://solarcyclescience.com/solarcycle.html).

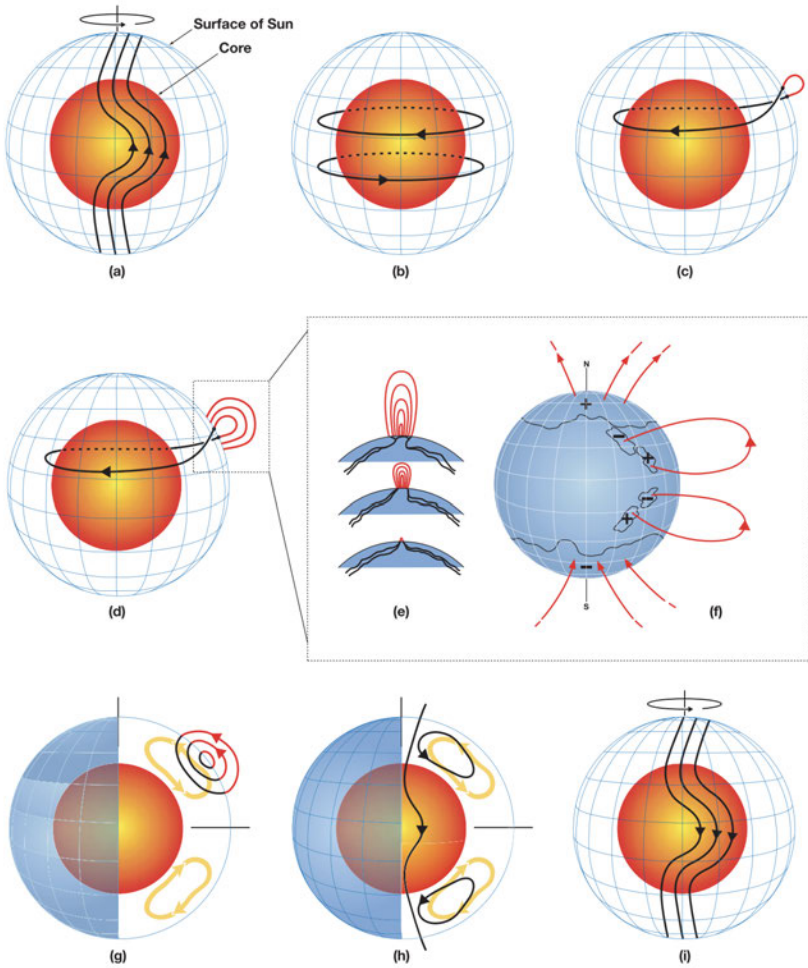

Fig. 2.7. Schematic of solar flux-transport dynamo processes. The red inner sphere represents the Sun's radiative core, and the blue mesh is the solar surface. In between is the solar convective zone where the dynamo resides. (a) Shearing of poloidal field by differential rotation near the convective zone bottom. (b) Toroidal field is produced as a result of the shearing by differential rotation. (c) When the toroidal field is strong enough, buoyant loops rise to the surface, twisting as they rise due to rotational influence. Sunspots are formed from these loops. (d)-(f) Additional flux emerges (panels d and e) and spreads (f) in latitude and longitude from decaying spots. (g) Meridional flow (yellow circulation with arrows) carries surface magnetic flux poleward, causing polar fields to reverse. (h) Some of this flux is then transported downward to the bottom and toward the equator. These poloidal fields have a sign opposite to those at the beginning of the sequence, in panel a. (i) This reversed poloidal flux is then sheared again near the bottom by the differential rotation to produce the new toroidal field opposite in sign to that shown in (b) [*Dikpati and Gilman*, 2009].

transports the magnetic flux poleward causing the polar magnetic field to reverse [*Dikpati and Gilman*, 2009].

2.5. Physics of the solar corona

Solar corona can be observed in visible light from the Earth during a solar eclipse when the intense direct light from the solar photosphere is occulted by the Moon. Figure 2.8 shows a white light photograph taken from the Earth during a solar eclipse in 2008. The solar corona can also be observed on the solar disk in extreme ultraviolet (EUV) or X-ray measurements. The solar corona is highly structured through the solar cycle by the global magnetic configuration of the Sun. On large scales, three different types of regions are distinguished: active regions (AR), quiet Sun (QS) and coronal hole (CH) regions. The pattern and the distribution of these regions also varies with the solar cycle (see Figure 2.9).

Active regions include concentrated magnetic flux tubes whose both ends are rooted in the Sun. These flux tubes appear brighter in EUV images due the higher density of the confined plasma than in the surrounding region. Active regions often include sunspot groups. Many dynamic phenomena such as flares [e.g., *Benz*, 2008; *Hudson*, 2011] and coronal mass ejections [e.g., *Thompson et al.*, 1998; *Gibson and Low*, 1998], occur in these regions. Coronal holes are regions where magnetic field lines reach far out into space forming a large part of the interplanetary magnetic field (IMF). Fast solar wind emerges from these open field line regions, with maximum velocities of 700 – 800 km/s, while slow solar wind has velocities on the order of 300 – 400 km/s. Quiet Sun regions form the third form of magnetic fields appears in the solar coronal disk, in addition to coronal holes and active regions. In the past, these regions were considered to be quiet in magnetic activity. With increased resolution of solar observations, considerable activity has been observed in these regions, e.g., in terms of bright points, small flares, small coronal mass ejections and jets [*Podladchikova et al.*, 2002; *Sánchez Almeida et al.*, 2010]. At solar maximum times the corona is visible all around the limb due to the wide latitudinal range over which ARs are located, while at solar minima the bright coronal structures only appear over the equator (Figure 2.8).

The open field lines of coronal holes are rooted in photospheric unipolar magnetic flux tubes emerging mainly in the dark lanes between the photospheric granulation cells [*Cranmer*, 2009]. Higher in the chromosphere, these network flux bundles are believed to undergo further broadening into so-called funnels [*Gabriel*, 1976; *Dowdy et al.*, 1986], which are considered to be the source region of the fast solar wind. Figure 2.10 illustrates the successive merging of flux tubes from granules to supergranules. Figure 2.10(a) is a zoom onto the photosphere where thin magnetic flux tubes concentrate in the dark lanes between photospheric granulation cells. Figure 2.10(b) shows the chromosphere at a larger scale than Figure 2.10(a). The funnels merge into a larger network field distribution [*Cranmer and*

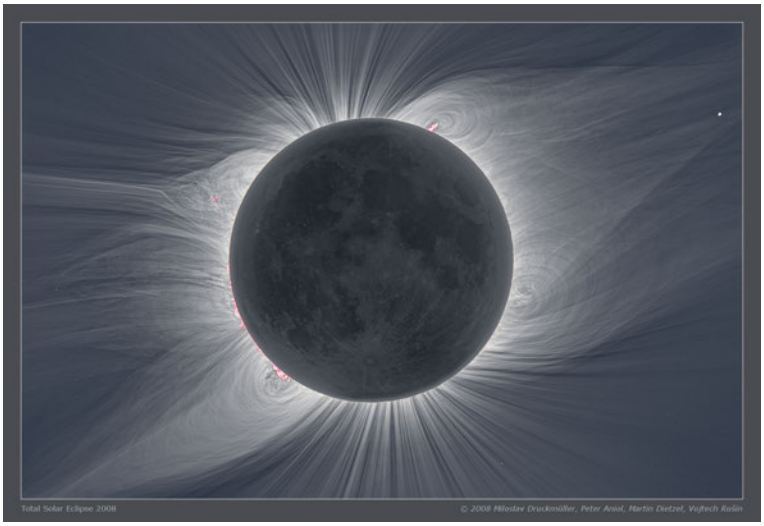

Fig. 2.8. High-resolution image of the solar corona during a solar eclipse observed in August 01, 2008. (Credit: Miloslav Druckmüller, Martin Dietzel, Peter Aniol, Vojtech Rušin)

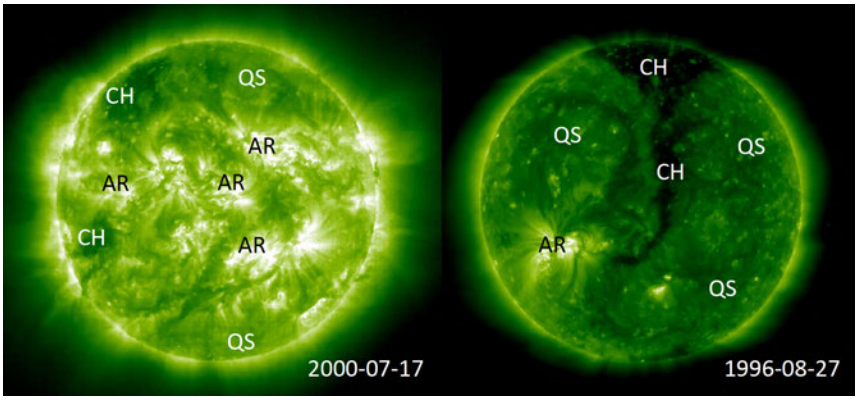

Fig. 2.9. Two SOHO/EIT images of the solar corona at 195Å at solar maximum/minimum times (left/right), respectively. Three different types of coronal regions are labeled: Active regions (AR), quiet sun (QS) and coronal hole (CH).

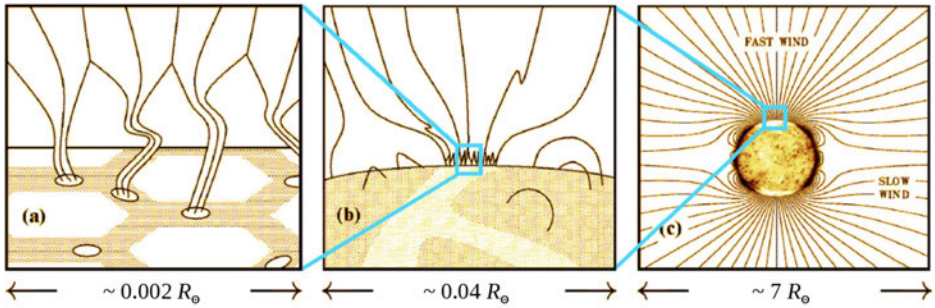

Fig. 2.10. A schematic of the open flux structure in a polar coronal hole with the field of view successively widening from flux tubes in intergranular lanes (a) to a funnel rooted in a supergranular network lane (b), and finally to the extended corona (c) [*Cranmer*, 2009].

van Ballegooijen, 2005]. This network is the supergranular network and has a typical size of about $0.04R_s$ or 27000 km. Finally, Figure 2.10(c) shows at global scales how the field extends into the corona. Hot coronal plasma in CHs cannot be confined on these open field lines and escapes from the corona along open field lines into the interplanetary space, and feeding the heliosphere with the solar wind [*Wilhelm et al.*, 2000] and reducing the density and pressure in the coronal hole.

Coronal holes exhibit a more rigid rotation [*Timothy et al.*, 1975] than the typical differential rotation at photospheric levels, and are linked to the global solar magnetic field. Consequently, they are often considered as indicators of the large-scale magnetic field in the solar corona [*Bumba et al.*, 1995]. *Bilenko and Tavastsherna* [2016] indicated that the longitudinal distribution of non-polar coronal holes follows the structure of the global magnetic field. Figure 2.11 shows the latitudinal profile of the rotation rate of coronal holes (black asterisks) with the red and purple curves obtained by fitting the hemispheric CHs using a parabola. The overlayed photospheric rotation profiles are estimated by two different methods from helioseismology [*Schou et al.*, 1998] and from Doppler shift measurements [*Snodgrass and Ulrich*, 1990]. Although the rotation rates of coronal holes at low latitudes are quite close to photospheric rotation rates obtained by helioseismology, the latitudinal variation of coronal hole rotation does not match with any of the photospheric rotation profiles.

Coronal holes have dynamic boundaries since field-line reconnection continually takes place in the corona. Thus, the coronal field configuration rearranges itself in response to the differential motion of the photosphere. The lifetimes of non-polar coronal holes were found to range from one solar rotation to more than 10 solar rotations, while the polar holes are even more persistent features around

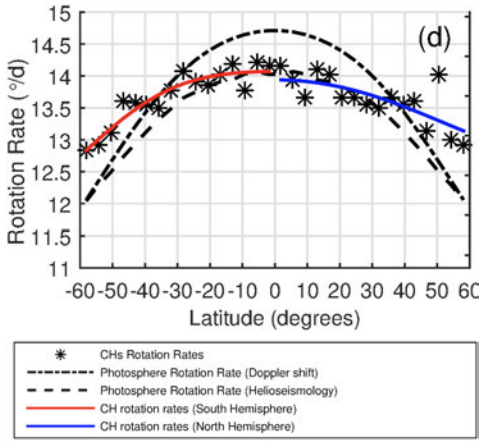

Fig. 2.11. CH sidereal rotation rates for 32 latitudinal zones (black cresses), and their corresponding curves fitted for each hemisphere separately. Black dot-dashed and dashed indicate the photospheric rotation rates obtained from Doppler shift measurements [*Snodgrass and Ulrich*, 1990] and from helioseismology, respectively. [*Schou et al.*, 1998]. Red (purple) curve corresponds to the rotation profile of CHs in the southern (northern) hemisphere [*Bagashvili et al.*, 2017].

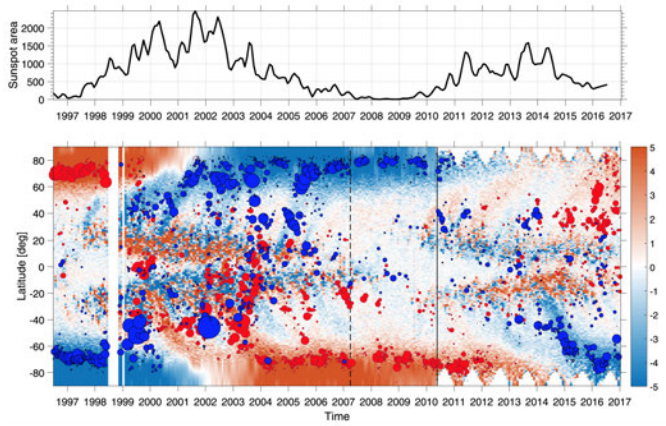

Fig. 2.12. CH evolution through Solar Cycles 23 and 24. Top panel: total sunspot area for reference. Bottom panel: the circles depict CH centroids with size proportional to the CH size on the solar surface. The color of the circle indicates the dominant polarity of the CH (red is positive polarity and blue negative). Background color indicates the average photospheric magnetic field intensity in units of Gauss. [Paper I].

solar minima. Coronal holes can be divided into polar and "equatorial" (actually low-to-mid latitude) CHs according to their latitudinal location on the solar disk. Their number, size, latitude distribution, temporal occurrence and evolution vary from cycle to cycle and during the same solar cycle [Paper I; see Fig. 2.12]. At solar minima, persistent, large coronal holes cover the two poles of the Sun with opposite magnetic polarities. These are polar coronal holes (PCHs). The area of PCHs is largest in the late declining to minimum phase of the solar cycle [*Harvey and Recely*, 2002; *Hess Webber et al.*, 2014; *Lowder et al.*, 2017]. During the minimum phase, PCHs typically extend down to a latitude of about 60° in each hemisphere [*Wang et al.*, 1996]. During the ascending phase, their area decreases with the increase of sunspots [*Bravo and Stewart*, 1996] until they disappear at the sunspot maximum [*Waldmeier*, 1981]. During solar maxima, coronal holes are frequently present as isolated regions all over the solar surface, also at low solar latitudes [*Cranmer*, 2009]. Non-polar coronal holes are often called "equatorial" coronal holes (ECHs). The total number and area of ECHs increase from the solar minimum towards the solar maximum [*McIntosh et al.*, 1992; *Bilenko*, 2002]. Soon after the solar maximum, during the declining phase of the solar cycle, polar coronal holes with magnetic polarity opposite to the previous solar cycle gradually begin to grow at the poles (see Fig. 2.12).

3. Solar observations and visualization

Since the beginning of the 1970s, several space missions have been carried out, supplied with instruments continuously observing the Sun with high spatial and spectral resolution in EUV. These observations provide images of the solar disk in different wavelengths which can be used to study various solar structures and their temporal evolution and to derive plasma parameters, such as the electron density, temperature, and velocity. This work uses observations from the Solar and Heliospheric Observatory (SOHO) probe and the Solar Dynamics Observatory (SDO) satellite, which will be discussed in this section. The period of operation of the two satellites are shown in Figure 3.1 together with the sunspot numbers.

3.1. Solar and Heliospheric Observatory

The Solar and Heliospheric Observatory is a solar-dedicated space mission aimed to observe the solar atmosphere and the photospheric magnetic field, and to provide imaging for helioseismology. It is operated by the European Space Agency (ESA) together with the National Aeronautics and Space Adminstration (NASA). SOHO was launched on 2 December 1995 and was then put into a halo orbit with a period of 180 days around the first Lagrangian point (L1) on 14 February 1996. The L1 point is located between the Sun and Earth and about 1.5 million kilometers away from the Earth, where the centrifugal forces and gravitational forces of Sun and Earth balance. Unlike observatories in an orbit around the Earth, SOHO can observe the Sun continuously without the visibility being blocked by the Earth.

We use here data from two instruments. SOHO/Extreme ultraviolet Imaging Telescope (EIT) is one of the solar atmosphere remote-sensing instruments used to study the physical processes that take place in the upper solar atmosphere. Michelson Doppler Imager (MDI) belongs to the helioseismology instruments which are responsible for measurements of solar oscillations with a high precision and accuracy.

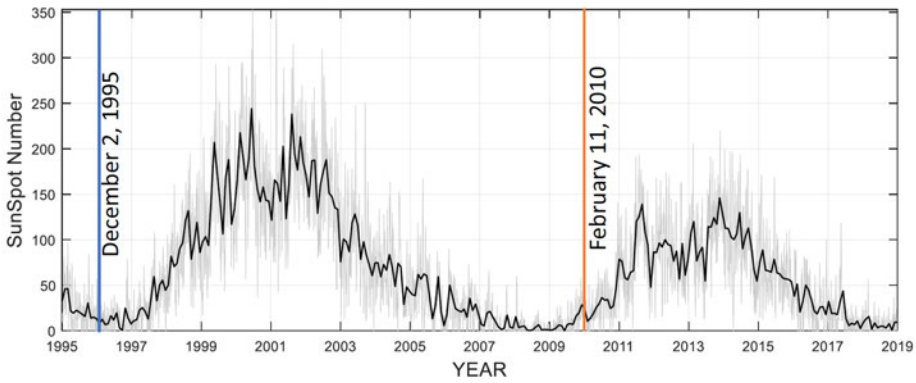

Fig. 3.1. Daily (grey) and monthly average (black) sunspot numbers over the solar cycles 23 and 24. The launch dates of SOHO and SDO satellites have been marked as vertical blue and red lines, respectively.

Table 3.1. SOHO/EIT wavelengths with related emission line and corresponding region in the solar atmosphere and temperature [*Delaboudinière et al.*, 1995].

Wavelength	Ion	Region of atmosphere	Peak Temp. (MK)
304Å	He II/Si XI	chromosphere, transition region	0.08
171Å	Fe IX/X	quiet corona, upper transition region	1.3
195Å	Fe XII	corona	1.6
284Å	Fe XV	active-region, corona	2.0

3.1.1. Extreme ultraviolet Imaging Telescope

EIT is a full-disk EUV imager of solar corona in four wavelengths (Fe IX/X 171Å, Fe XII 195Å, Fe XV 284Å and He II/Si XI 304Å) as shown in Figure 3.2. Table 3.1 shows SOHO/EIT wavelengths and the corresponding ion emission lines, regions and temperatures. EIT is equipped with a 1024×1024 pixel CCD camera. Each pixel size corresponds to 2.6 arcsec spatial resolution. A detailed description of this instrument is given by *Delaboudinière et al.* [1995]. During the SOHO mission, EIT has been used to observe polar and equatorial coronal holes on the solar disk. Coronal holes appear as dark features in the EIT full-disk images obtained in its four coronal channels.

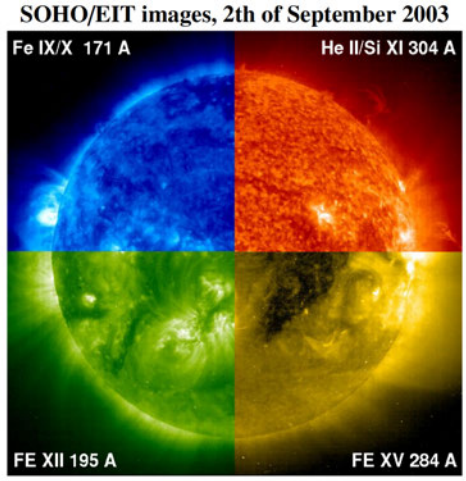

Fig. 3.2. SOHO/EIT solar image assemblage in four wavelengths (Fe IX/X 171Å, Fe XII 195Å, Fe XV 284Å and He II/Si XI 304Å). Image credit: thesuntoday.org

3.1.2. Michelson Doppler Imager

The MDI instrument [*Scherrer et al.*, 1995] was built to probe the solar interior using helioseismological techniques and to measure the line-of-sight magnetic field component. MDI measures the Doppler shift in right and left-handedly circularly polarized light from the Ni I 6768Å absorption line which forms at about 200–300 km above the photosphere [*Georgobiani et al.*, 2000]. These MDI measurements provide full-disk solar images of line-of-sight magnetic field (Figure 3.3) every 96 minutes with a total field of view of 34×34 arcminutes [*Scherrer et al.*, 1995]. The accuracy of the magnetic field data is about 20 G. The detector is a 1024×1024 pixel CCD, which can operate at 2 or 0.6 arcsec pixel resolution.

3.2. Solar Dynamics Observatory

Solar Dynamics Observatory is a spacecraft for solar observations launched on February 11, 2010 and operated by NASA. SDO arrived at the geosynchronous orbit on March 16 , 2010. The main objective of SDO is the observation and study of solar dynamics, especially solar flares, coronal mass ejections (CMEs) and solar wind in connection to space weather. For this reason, SDO is mounted with multiple instruments (see Figure 3.4). From the SDO spacecraft, data of the Atmospheric Imaging Assembly (AIA) and Heliospheric and Magnetic Imager (HMI) are used in this work.

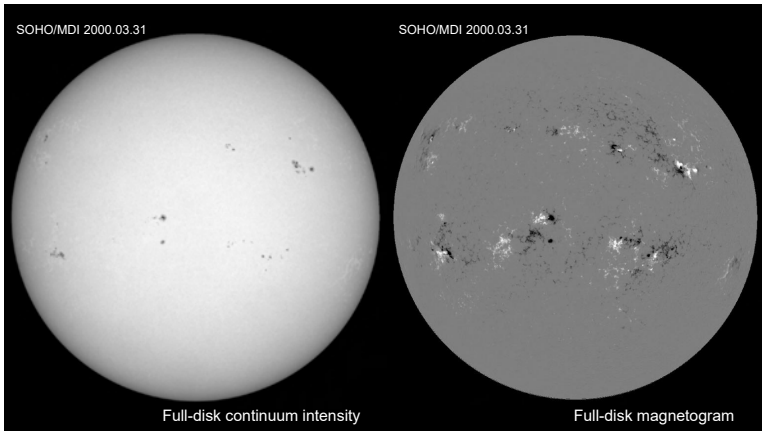

Fig. 3.3. Full-disk continuum intensity image (left) and magnetogram image (right) of the Sun from SOHO/MDI on March 31, 2000.

3.2.1. Atmospheric Imaging Assembly

The Atmospheric Imaging Assembly [*Lemen et al.*, 2011] is a telescope array with 4096×4096 pixel CCD observing the Sun at 7 wavelengths in EUV (304Å, 171Å, 193Å, 211Å, 335Å, 94Å, 131Å) and 3 in UV/visible (white light, 1700Å, 1600Å). These wavelengths correspond to different ion transitions at different temperatures and thus different heights above the solar surface (Table 3.2). Figure 3.5 shows the Sun as observed by SDO in all these wavelengths. The field of view extends to 1.5 R_s from the centre of the solar disk. The spatial resolution is 1.5 arc-seconds and the cadence is 12 seconds.

The formation temperature of the Fe XII ions that radiate in the 193Å wavelength is $1.4 - 1.6 \times 10^6$ K [*Aschwanden et al.*, 2013; *Lemen et al.*, 2011]. This wavelength is particularly good for observing CHs as they are clearly visible as dark structures in the 193Å spectral line. CHs are also clearly visible in the 171Å and the 211Å lines. *Hofmeister et al.* [2017] have shown that the extraction of dark coronal structures, especially CHs, works very consistently in the 193Å images. *Inglis et al.* [2019] used a sequential manual inspection of 211Å and 193Å to identify and characterize four examples of the ephemeral CHs.

Table 3.2. SDO/AIA wavelengths with related emission line, corresponding region in the solar atmosphere and temperature [*Lemen et al.*, 2011].

Wavelength	Ion	Region of atmosphere	Peak Temp. (MK)
4500Å	continuum	photosphere	0.005
1700Å	continuum	photosphere, temperature minimum	0.005
304Å	He II/Si XI	chromosphere, transition region	0.08
1600Å	C IV + cont.	transition region, upper photosphere	0.1
171Å	Fe IX/ X	quiet corona, upper transition region	1.3
193Å	Fe XII/ XXIV	corona and hot flare plasma	1.6
211Å	Fe XIV	active-region, corona	2.0
335Å	Fe XVI	active-region corona	2.5
94Å	Fe XVIII	flaring corona	6.3
131Å	Fe VIII/ XXI	transition region, flaring corona	0.4

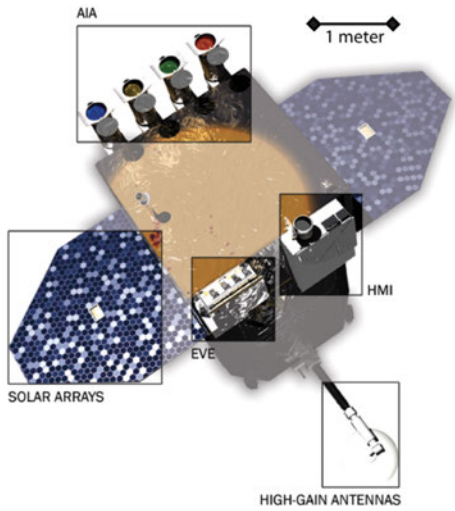

Fig. 3.4. The SDO spacecraft with its three instruments (AIA, HMI, EVE), high-gain antennas, and solar arrays highlighted. From *Pesnell et al.* [2012].

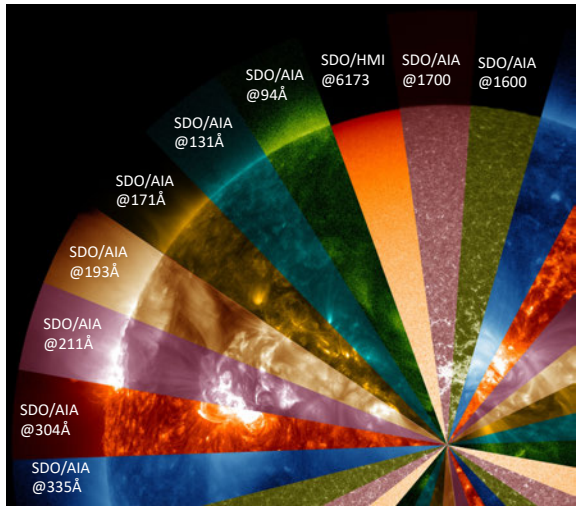

Fig. 3.5. The Sun as observed by SDO/AIA in different wavelengthes. The image is pseudo-colored. The Sun with an overlay of different filters with the wavelength from left to right: 335Å, 304Å, 211Å, 193Å, 171Å, 131Å, 94Å, 6173Å, 1700Å, 1600Å. Adapted image from NASA (https://www.nasa.gov).

3.2.2. Heliospheric and Magnetic Imager

Heliospheric and Magnetic Imager (HMI, *Hoeksema et al.* [2014]) provides full-disk magnetic field observation as well as internal flows, vector magnetic field, photospheric surface velocity measurements with an image size of 4096×4096 pixels and spatial resolution of around 1 arc-second [*Schou et al.*, 2012]. HMI uses the 6173Å Fe I absorption line to measure surface velocity using the Doppler shift of the line. Full-disk images of the velocity measurements (dopplergrams) are created every 45 seconds with a resolution of 0.5 arc-second. The Zeeman effect of the 6173Å Fe I line is used to calculate the Stokes polarization parameters which allows the full magnetic field vector estimation [*Pesnell et al.*, 2012; *Schou et al.*, 2012].

3.3. Solar synoptic maps

The Sun can be visualized in many different ways. The most common are the full-disk images (see Figures 2.8, 2.9, 3.3) where the whole visible solar disk is captured using ground or space-based telescopes. In these images, the Sun is positioned at the centre of the image and the axis units are usually in arc-second. These obser-

vations are limited to the visible side of the Sun, while the far side is not visible. Such observations are beneficial in the immediate solar analysis. Another type of solar visualization is the synoptic (or Carrington) map. Synoptic maps provide a convenient way to display the distribution/evolution of various physical quantities and long-lived features on the entire solar surface. For example, synoptic maps have been used to study coronal holes [*Karna et al.*, 2015; *Hamada et al.*, 2018], photospheric and coronal magnetic fields [*Virtanen and Mursula*, 2016], and the distribution/development of long-lived active regions [*Golubeva and Mordvinov*, 2017]. Solar synoptic maps can also be used to study the nonuniform structure of the EUV corona in both longitude and latitude, reflecting the nonuniform distribution of the large-scale magnetic field [*Benevolenskaya et al.*, 2001].

Each synoptic map is constructed by concatenating a series of meridian strips taken from full-disk images projected to heliographic coordinates and spanning a full Carrington Rotation (CR) of 27.2753 days. Each individual full-disk image is remapped into heliographic coordinates with longitude along the x-axis, and sine or linear latitude along the y-axis (Figures 3.6, 3.7). Rigid solar rotation is assumed in order to reduce the complication of the dynamic surface of the Sun [*Harvey and Worden*, 1998].

Currently, there are two other EUV synoptic map datasets based on SOHO/EIT observations and one synoptic map dataset based on SDO/AIA observations. *Benevolenskaya et al.* [2001] constructed SOHO/EIT synoptic maps in four wavelengthes (304Å, 171Å, 195Å, 284Å) from CR 1911 (June 28, 1996) to CR 2055 (March 31, 2007) by concatenating 16° wide central solar meridian strips. The size of these synoptic maps is 360 × 167 pixels with a resolution of 1° × 1° of heliographic longitude and latitude, covering all longitudes (1° to 360°) and most latitudes (−83° to +83°, leaving out those polar latitudes that are not always visible due to Earth's inclined orbit around the Sun). These EIT synoptic maps are provided by Stanford Solar Observatories Group (SSOG) (`http://sun.stanford.edu/synop/EIT/index.html`). Another set of SOHO/EIT synoptic maps for only three wavelengths (304Å, 171Å and 195Å) are provided by the Space Weather Lab (SWL) at George Mason University (`http://spaceweather.gmu.edu/projects/synop/EITSM.html`) [*Hess Webber et al.*, 2014]. The available maps extend from CR 2058 (June 21, 2007) to CR 2102 (October 03, 2010). In the SWL maps, central meridian longitudinal strips of 13.63° width have been concatenated using four images per day with 3/4 overlap between adjacent strips. The size of these synoptic maps is 3600 ×1080 pixels (0.1° × 0.1667°) and they cover all longitudes and all measured latitudes at best up to ±90°. There are many missing and gappy maps in this dataset (23 out of 45 CRs).

The only dataset of SDO/AIA synoptic maps is provided by SWL (`http://spaceweather.gmu.edu/projects/synop/AIASM.html`) from CR 2097 (May 20, 2010) to CR 2186 (January 10, 2017) [*Karna et al.*, 2014]. These dataset has been recently extended to CR2228 (March 01, 2020). The resolution and latitudinal extent is the same as that of SWL/EIT synoptic maps (and also made of 13.63°

Table 3.3. Data coverage of previous dataset of SOHO/EIT and SDO/AIA EUV synoptic maps

Source	Observable	Start		End	
		CR	Date	CR	Date
SSOG	SOHO/EIT: 284Å, 195Å, 171Å, 304Å	1911	1996.06.28	2055	2007.03.31
SWL	SOHO/EIT: 195Å, 171Å, 304Å	2058	2007.06.21	2102	2010.10.03
SWL	SDO/AIA: 193Å, 171Å, 304Å	2097	2010.05.20	2186	2017.01.10

wide central solar meridian strips). Also, these maps are provided only for three wavelengths (304Å, 171Å and 193Å). The maps from CR 2097 (May 20, 2010) to CR 2124 (May 25, 2012) are available in sine and linear latitude while the maps from CR 2125 (June 21, 2012) to CR 2186 (January 10, 2017) are available in linear latitude only. The temporal coverage of these three databases of SOHO/EIT and SDO/AIA synoptic maps are summarized in Table 3.3. Many maps contain data gaps and sharp edges between adjacent longitudinal strips. Maps of some wavelengths are missing for some Carrington rotations. For SWL/AIA maps, it also seems that the camera's exposure time and the image quality key-factors are not always taken into account in the synoptic map preparation, which is seen as overexposed (or underexposed) strips in the synoptic maps.

In Paper III, we present a new homogenized dataset of EUV synoptic maps, based on SOHO/EIT and SDO/AIA observations. These maps are constructed homogeneously in standardized intensity scale with the same methodology (using daily 13.3° wide central solar meridian strips) for both instruments and finally inter-calibrated to eliminate the differences in intensity distribution between the two instruments.

Figure 3.7 shows how we have constructed the synoptic maps (Figure 3.7d) by including all the projected full-disk images belonging to the corresponding Carrington rotation, taking from each the 13.3° wide central meridian strip and overlapping the neighbouring strips by half of their width. The overlapping parts (Figure 3.7a, b) are averaged using a linearly varying weighting function (Figure 3.7c) that drops from one at strip center to zero at the strip edge. This linear function is introduced to get rid of the sharp edges between different strips. In comparison to the existing SOHO/EIT and SDO/AIA synoptic map datasets from SSOG and SWL, the new maps constructed here provide a longer and more homogeneous dataset with fewer data-gaps.

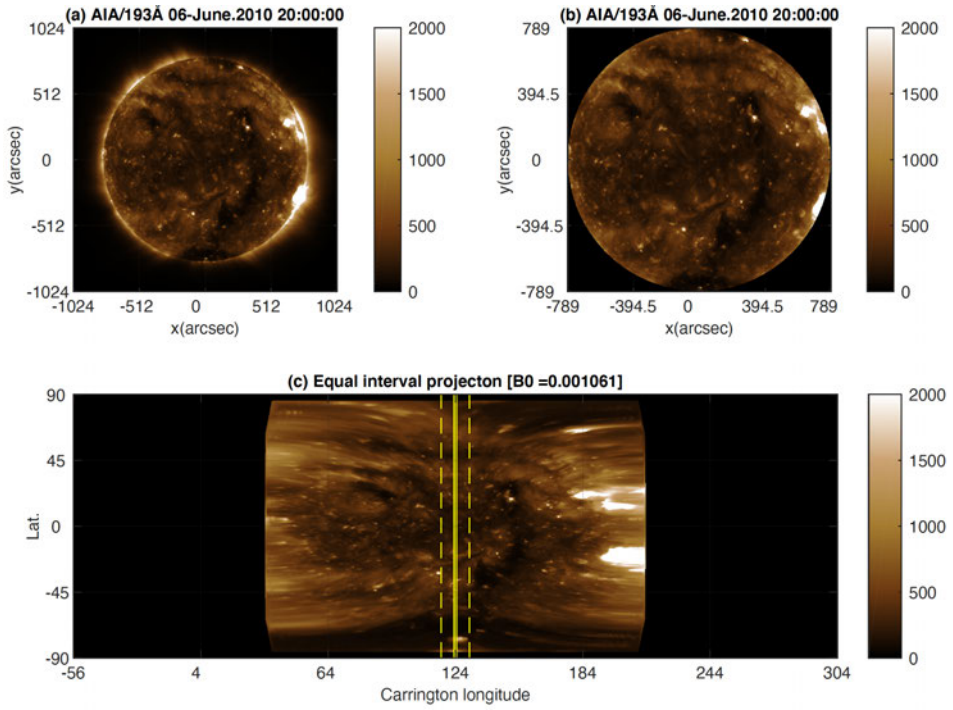

Fig. 3.6. (a) Full-disk AIA/193Å image taken on 2010 June 06. (b) The same with all off-limb pixels removed. (c) Full-disk image projected from image plane to heliographic coordinates. Vertical yellow dashed lines denote the 13.3° wide central solar meridian strips. [Paper III].

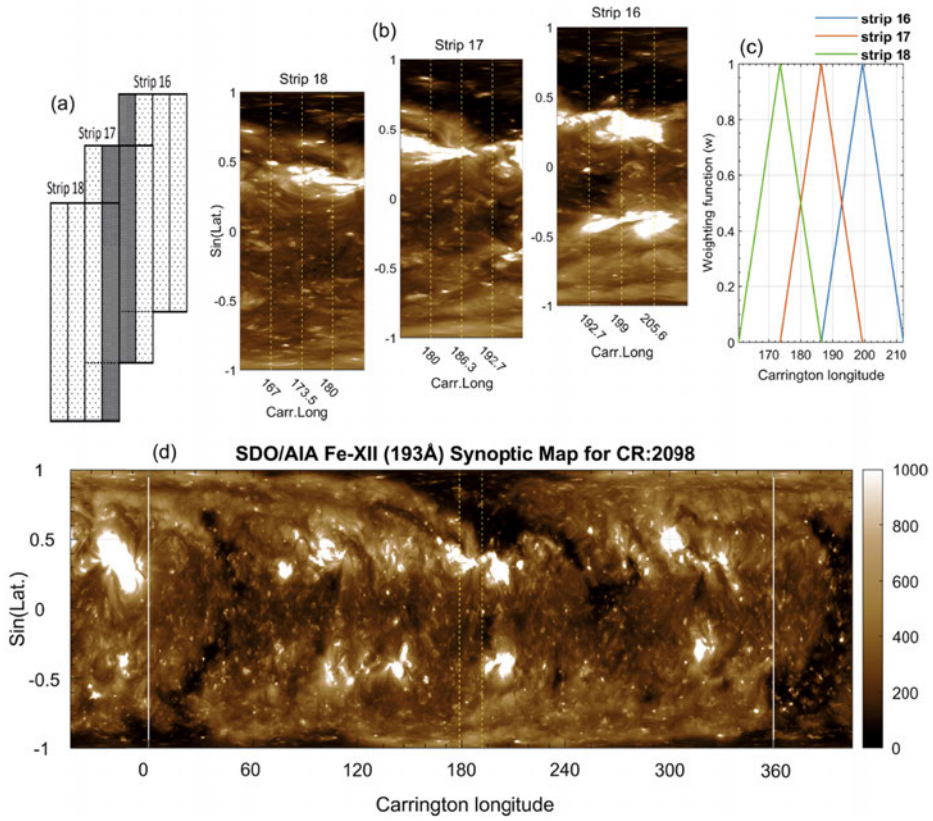

Fig. 3.7. The synoptic map is made by averaging central longitude strips (of 26.6° wide) taken from successive daily full-disk images projected to heliographic coordinates, with a half strip-width overlap between adjacent strips. (a) Three successive daily meridian strips 16, 17, and 18. The shaded area represents the overlapping parts. (b) The same EUV meridian strips where the shaded area is located within the vertical yellow solid lines. (c) The corresponding linear weighting function for strips 16, 17, and 18. (d) EUV synoptic map for CR 2098. Vertical white solid lines represent the map boundaries. [Paper III].

4. Coronal hole identification

The boundaries of coronal holes, as defined by the solar EUV images are rather complicated. The area, shape, and darkness of any given hole are not the same in different wavelengths [*Kahler et al.*, 1983; *Harvey and Recely*, 2002]. In the photosphere and low chromosphere, the density difference is less pronounced. Therefore, in the photosphere, coronal holes are hardly distinguishable from their surroundings [*Cranmer*, 2009]. Foreground coronal emission may frequently hide a coronal hole or give a systematic displacement of its boundaries from their true surface locations, especially for a hole far from the disk center [The Wall Effect: *Hess Webber et al.*, 2014]. Also, magnetic interactions near the boundaries may result in a diffuse boundary of the coronal hole [*Kahler and Hudson*, 2002]. This makes the CH boundaries unsharp and partly obscured by magnetic structures related to surrounding active regions.

Coronal holes were first observed by *Waldmeier* [1957] who noticed long-lived regions of negligible intensity in coronagraphic images of the 5303Å green line. In the 1970s, CHs were observed as discrete dark patches in the X-ray and EUV solar disk images [*Krieger et al.*, 1973; *Zirker*, 1977]. *Harvey and Recely* [2002] manually identified coronal holes from NSO/Kitt Peak Vacuum Telescope (KPVT) He I 10830Å synoptic spectroheliograms created from full-disk observations (Figure 4.1). They determined the CH threshold intensity as the 15/85th percentile of intensity. Methods based on a fixed intensity threshold at one wavelength [*Abramenko et al.*, 2009] have been found to be insufficient [*de Toma*, 2011] because the CH threshold intensity may vary with time. There have been several attempts to automate the identification and detection of CHs using different techniques, such as edge-based segmentation [*Scholl and Habbal*, 2008], perimeter tracing [*Kirk et al.*, 2009], multichannel fuzzy clustering [*Barra et al.*, 2009], and intensity thresholding [*Krista and Gallagher*, 2009; *de Toma*, 2011]. Although the CH intensity threshold is fundamentally important when determining CH boundaries, many of these methods chose the CH threshold rather arbitrarily. The spatial possibilistic clustering algorithm (SPoCA; *Verbeeck, C. et al.* [2014]) utilizes fuzzy clustering algorithms and distinctions on area and lifetime of features to differentiate CHs from other features. Recently, machine learning algorithms were used in order to

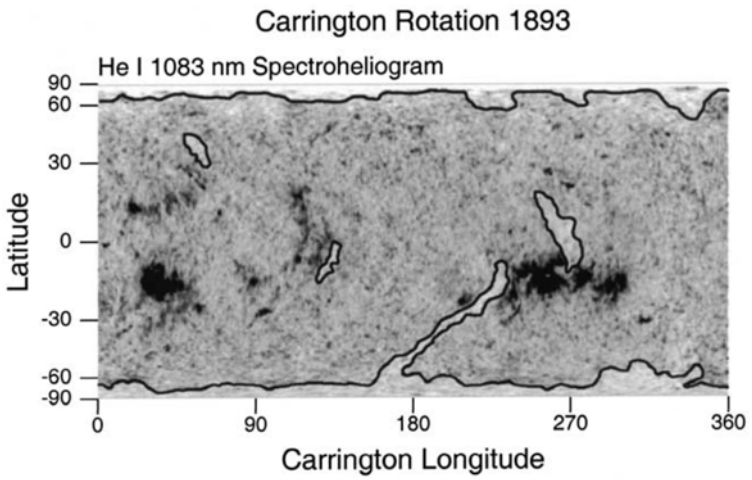

Fig. 4.1. Synoptic map of He I 10830Å spectroheliogram. He I 10830Å intensity is displayed as inverse equivalent width. The boundaries of two polar holes, the southern polar hole forming an equatorial extension, and three isolated holes are outlined by the heavy black curves [*Harvey and Recely*, 2002].

distinguish CHs [*Reiss et al.*, 2015; *Illarionov and Tlatov*, 2018].

4.1. Coronal hole identification method

In paper I we developed a new methodology for automatically identifying coronal holes. The identification of coronal holes is based on studying the synoptic map in small square segments with segment length varying from 15 to 55 pixels in nine 5-pixel steps. These synoptic maps have a resolution of $1^\circ \times 1^\circ$ of heliographic latitude and longitude. The optimal segment for coronal hole identification is the one which most clearly depicts the separate coronal hole and quiet Sun populations in a bimodal histogram (Figure 4.2) with as large a contrast as possible and as low a mean intensity as possible. Figure 4.2 depicts an example of an EUV synoptic map (1996 June 29) with an optimal segment denoted by a rectangle with yellow borders. The histogram of the segment is clearly bimodal, consisting of two distinct, but partly overlapping distributions: the darker coronal hole and the brighter quiet Sun. Note also that the histogram of the full map barely shows any clear sign of coronal holes. The contrast of the segment represents the difference between the population of dark pixels and the population of the brighter ones. Finding the optimal segment from segments of different sizes allows the algorithm to adjust to the spatial scale of coronal holes, which varies over time. The coronal

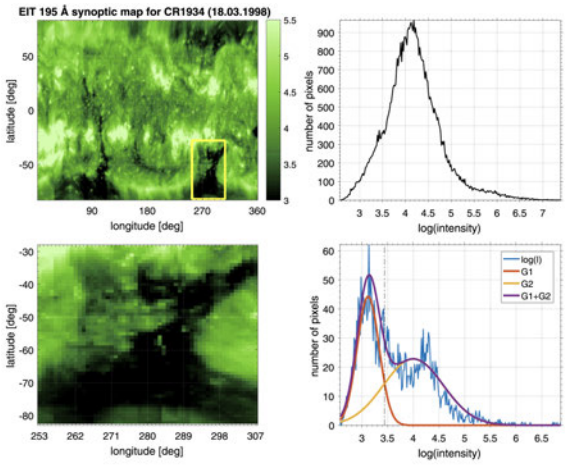

Fig. 4.2. EIT 195Å synoptic map for CR 1934 (1998 March 18) and its intensity distribution (upper panels). The yellow box indicates the optimum segment of length l = 55. An expanded view of the yellow box and its intensity histogram are shown in the lower panels. The segment histogram was fit to a sum of two Gaussians shown in the lower right panel. The vertical dash-dotted line indicates CH threshold intensity [Paper I].

hole threshold intensity was then defined as the intersection between these two Gaussians [Paper I].

After determining the final coronal hole threshold intensities of the three different wavelengths (195 Å, 171 Å, and 304 Å), they are used to produce binary maps of coronal holes by marking the pixels with intensity lower than the threshold as 1 and those with higher intensity as 0. Examples of such initial binary maps are shown in Figure 4.3b, where white regions indicate coronal holes. The binary maps were then post-processed by applying morphological image analysis functions of dilation and erosion with a 5×5 pixel square kernel. Most small structures will thereby be removed and the small gaps in the CH regions will be filled up (Figure 4.3c). As a coronal hole appears differently in different wavelengths, a composite distribution of CHs is produced by taking the median of the morphologically filtered binary CH maps from the three wavelengths. This approach yields a more robust result than using measurements only from one wavelength, which most earlier CH detection methods do. The most consistent CH regions between the three different wavelengths were obtained for polar regions, while the low-latitude CH regions were often quite different.

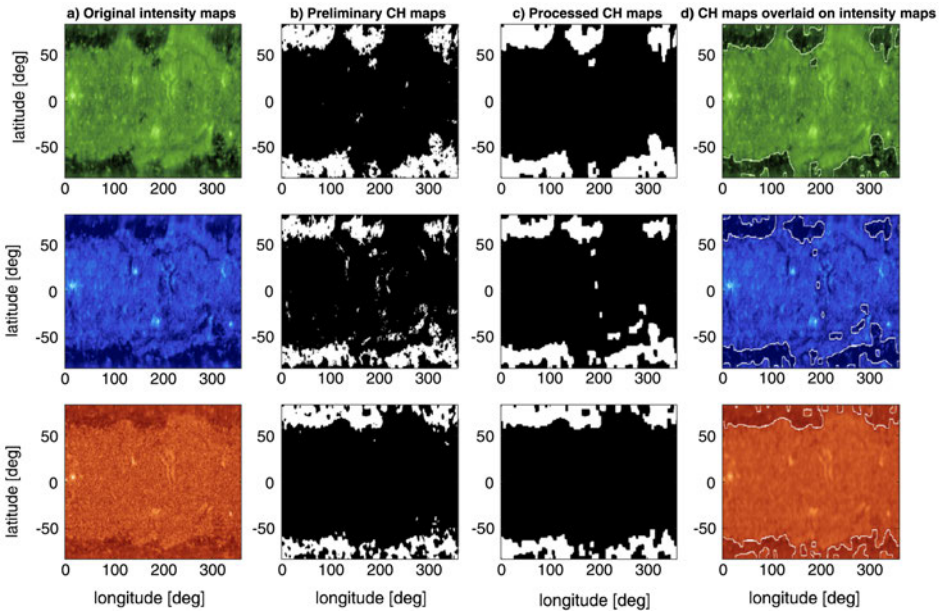

Fig. 4.3. Example of automated CH detection for CR 1922 (1997 April 24). Column (a) SOHO/EIT synoptic maps for 195 Å (green), 171 Å (blue), and 304 Å (red). Column (b) Preliminary binary CH maps after determining the CH intensity threshold. Column (c) Fully processed CH binary maps. Column (d) Edged CH areas overlaid on the EUV maps. The x and y axes depict heliographic longitude and latitude, respectively [Paper I].

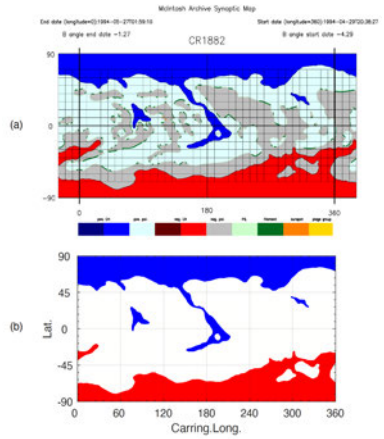

Fig. 4.4. (a) Example of a digitized, colorized McA synoptic solar map around CR1882 (April 04, 1994) with negative (gray) and positive (light blue) polarity magnetic fields, negative (red) and positive (dark blue) coronal holes, and filaments (green). (b) Extracted coronal hole synoptic map for CR1882.

Table 4.1. The three CH datasets used for comparison

Observable	Start		End	
	CR	Date	CR	Date
SDO/AIA: 193Å	2097	2010.05.20	2220	2019.08.21
SOHO/EIT: 195Å	1911	1996.06.28	2212	2018.12.20
KPNO/McA: He-I 10830Å	1601	1973.05.05	2086	2009.07.23

4.2. Comparison of coronal hole datasets

One of the longest running coronal hole datasets exists in the McIntosh Archive (McA) which consists of hand-drawn Carrington maps based on He-I 10830Å solar observations from Kitt Peak National Observatory (KPNO)[*Gibson et al.*, 2016]. These maps contain the positional and polarity information of different coronal holes together with various other solar features (Figure 4.4a). Coronal hole information (Figure 4.4b) is available in the McIntosh Archive from 1973 - 2009 (Table 4.1).

Based on the new homogenized EUV synoptic maps of EIT/195 Å and AIA/193 Å wavelengths (Figure 4.5a-b) [Paper III], the automated coronal hole identification algorithm developed in Paper I was used to construct the coronal hole synoptic maps (Figure 4.5c-f). Based on EIT/195 Å observations, the coronal hole synoptic

maps cover the years 1996-2018, covering the last two solar cycles 23 and 24 while the coronal hole synoptic maps based AIA/193Å span from 2010 untill the present, covering the solar cycle 24 (Table 4.1).

By calculating the fractional areas of the two polar coronal holes ($\pm 55°$:$\pm 90°$) and of the equatorial coronal holes ($+55°$:$-55°$), a characteristic time series for each CH region is obtained (Figure 4.6). There is a dramatic difference in the polar coronal hole areas between the manually identified McIntosh dataset and the automated identified dataset. (Figure 4.6a,b; Paper IV). In McIntosh dataset (Figure 4.4a), the maps are constructed manually by experienced observers who take into account the vantage point (B_0) effect to produce much larger and more continuous polar coronal hole areas during the decaying to minimum phase of the solar cycle. On the other hand, the automated CH identification algorithm [Papers I and IV] uses the EUV synoptic maps where the B_0 (vantage point) effect is an inherent problem within the pixel intensity distributions.

Figure 4.6c shows the rotational fractional areas of equatorial coronal holes (between latitudes $+55°$:$-55°$), as a function of time for each dataset. All the time series of the equatorial coronal hole areas are quite consistent with each other during the times when they overlap. Accordingly, the EIT/195Å and AIA/193Å observations can be used to reliably continue the MacIntosh archive coronal hole database at non-polar latitudes. We note that, the equatorial coronal holes have a cycle maximum in the early to mid-declining phase. Note also that the maximum ECH areas during a cycle are roughly similar for the higher cycles 21-23, but only half of that for the weak cycle 24.

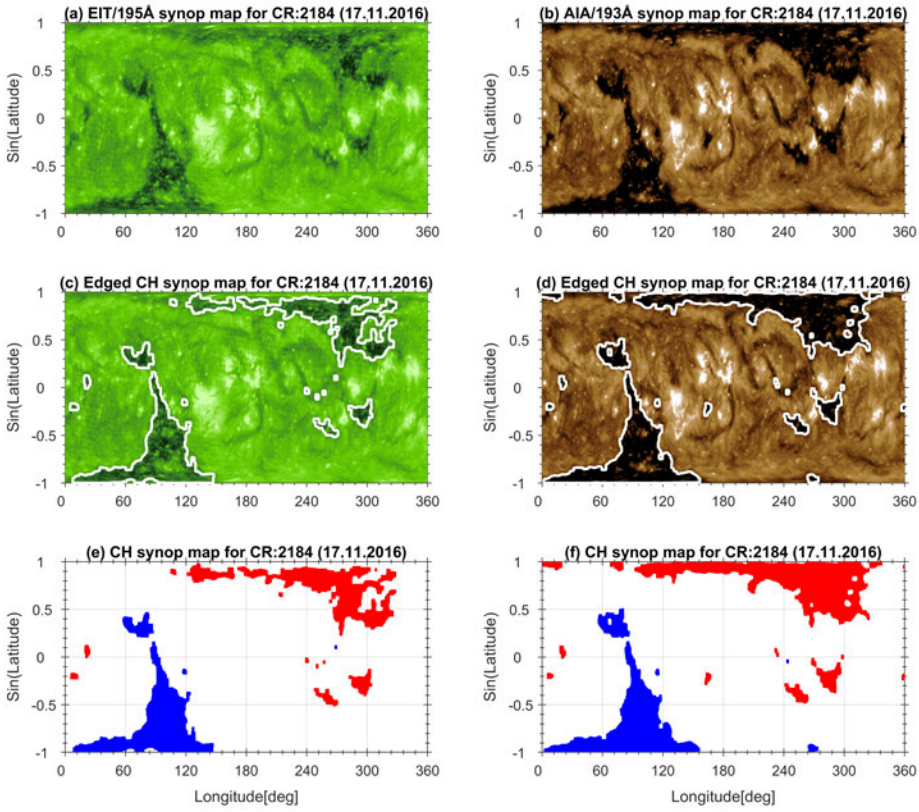

Fig. 4.5. Homogenized EUV synoptic map of (a) EIT/195Å and (b) AIA/193Å for CR 2184 (November 17, 2016). Coronal hole areas are extracted from the corresponding edged maps (c, d). Coronal hole binary maps based on (e) EIT/195Å and (f) AIA/193Å observations where the red/blue represents the positive/negative magnetic polarity, respectively.

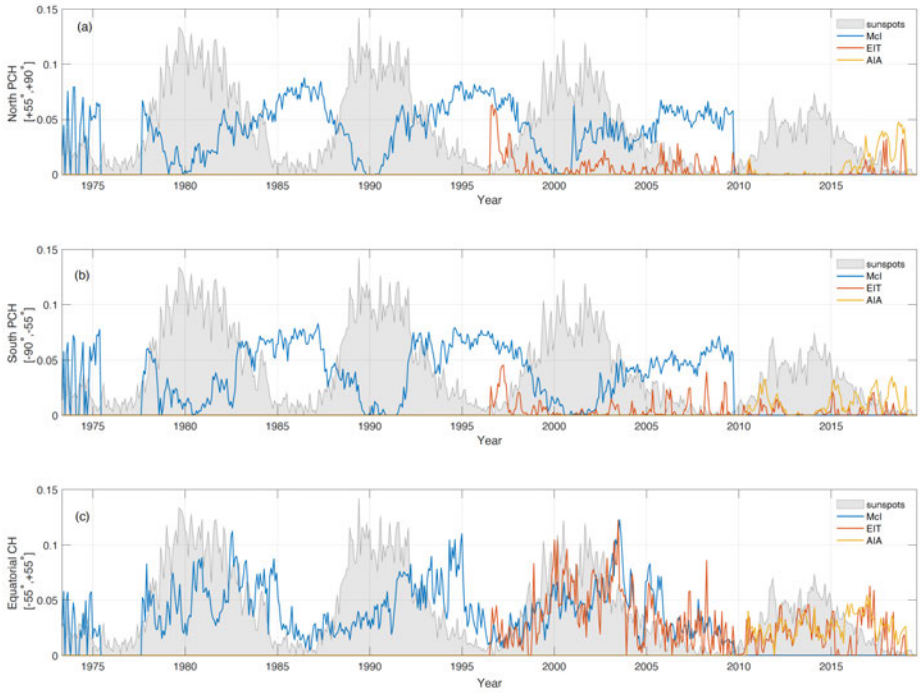

Fig. 4.6. Time series of fractional areas of coronal holes (averaged over Carrington rotations) with monthly sunspot numbers in the background. Northern (a) and southern (b) polar coronal hole (PCH) areas between latitudes $\pm 55^\circ$ and $\pm 90^\circ$, from McIntosh (blue), EIT/195Å (red) and AIA/193Å (yellow) dataset (c) Equatorial coronal hole (ECH) areas between latitudes $+55^\circ$ and -55°.

5. High-speed solar wind streams and geomagnetic activity

Solar wind is a continuous stream of particles (mainly protons and electrons as well as a few percent of alpha particles and heavier ions) escaping from the solar atmosphere, carrying the interplanetary magnetic field (IMF) and filling the surrounding interplanetary space. Continuous solar wind was suggested, based on comet tail observations by *Biermann* [1951], theoretically motivated by *Parker* [1958] and finally confirmed by direct measurements in the early 1960's [*Gringauz et al.*, 1960; *Snyder et al.*, 1963]. Solar wind observations by the Ulysses probe [*Geiss et al.*, 1995; *Woch et al.*, 1997; *McComas et al.*, 2000] showed how the solar wind speed is varying with heliographic latitude (Fig. 5.1). As the magnetic field in the coronal holes has an open configuration [*Zirker*, 1977], it allows the coronal plasma to become supersonic within several solar radii, giving rise to high-speed solar wind streams (HSS) [*Krieger et al.*, 1973].

During the solar minimum, fast solar wind with speeds of about 750 km/s emanating from polar coronal holes were found to be dominant (Figure 5.1, Ulysses first and third orbits). During the declining phase of the solar cycle, PCHs expand and exhibit large extensions to low heliographic latitudes. Therefore, high-speed solar wind streams are directed more often toward the Earth in the declining phase of the solar cycle [*Bame et al.*, 1976; *Manoharan*, 2012]. The polarity of the IMF associated with HSSs agrees with the dominant polarity of the photospheric magnetic field underlying the corresponding CHs [*Hundhausen*, 1977]. The velocities of the HSSs observed at 1 AU appear to be closely related with the size of the corresponding CH [*Nolte et al.*, 1976]. As new solar cycle starts, new active regions emerge and isolated holes start to emanate all over the solar disk, while the PCHs start shrinking [*Luhmann et al.*, 2002]. During the solar maximum (Figure 5.1, Ulysses second orbit), the solar wind speed above the south pole was reduced to be about 400 km/s, indicating the southern CH was replaced by large active region complexes.

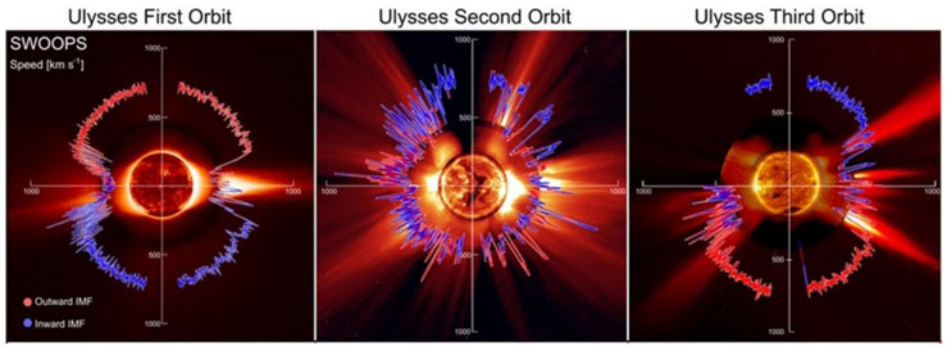

Fig. 5.1. Polar plots of solar wind speed as a function of latitude for the three solar orbits of the Ulysses spacecraft. The first orbit was around the solar minimum of cycle 22, the second during the solar maximum of cycle 23, and the third during the declining phase of cycle 23 [*McComas et al.*, 2003].

5.1. Co-rotating interaction regions

During its journey through interplanetary space, a high-speed stream can overtake and interact with the pre-existing low-speed solar wind, producing a recognizable pattern of compression, rarefaction, and shock in the plasma density and magnetic field (Figure 5.2), which is called the co-rotating interaction region (CIR) [*Belcher and Davis*, 1971]. The passage of such corotating interaction regions past the Earth's magnetosphere contributes to geomagnetic storm activity [*Kilpua et al.*, 2017]. Although only a small fraction of intense storms appear to be caused by HSS/CIRs [*Gosling et al.*, 1991; *Huttunen et al.*, 2002; *Zhang et al.*, 2007], they are responsible for a large fraction of moderate-strength storms [*Verbanac et al.*, 2011; *Echer et al.*, 2013]. HSS/CIR events efficiently heat the Earth's ionosphere and thermosphere [*Sojka et al.*, 2009], which can enhance spacecraft drag and alter its infrared energy budget. HSS/CIRs are significant as they can persist over long times (from a few days to a couple of weeks) and are likely to repeat over multiple solar rotations [*Sibeck and Richardson*, 1997; *Borovsky and Denton*, 2006].

The areas of equatorial CHs and PCH extensions are good indicators for HSSs and related CIRs [*Tsurutani et al.*, 1995, 2006; *Cranmer*, 2009; *Verbanac et al.*, 2011; *Borovsky and Denton*, 2013]. In fact, HSS/CIRs are the most dominant source of geomagnetic disturbances on the Earth causing a long-lasting and recurrent geomagnetic activity [e.g., *Vršnak et al.*, 2007]. Due to their frequent occurrence, the role of high-speed streams is more important for geomagnetic activity in the long run [*Richardson and Cane*, 2012; *Holappa et al.*, 2014].

Figure 5.3 shows the daily solar wind speed (Figure 5.3b) together with the

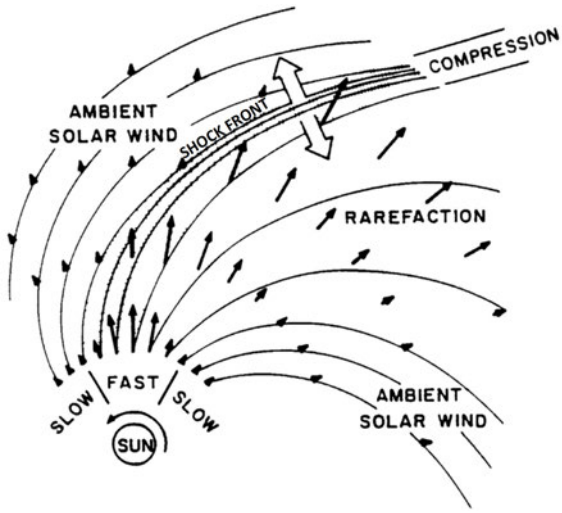

Fig. 5.2. A corotating interaction region (CIR) in the solar equatorial plane caused by the interaction of slow and high-speed solar wind streams [*Pizzo*, 1978].

monthly number of CME and HSS/CIR related flows (Figure 5.3c and d) in 1981-2016 [*Richardson and Cane*, 2012]. The number of CME-related events is maximized during solar maximum times, while the number of HSS/CIR-related events is maximized during the declining to minimum phase of the solar cycle. The last two panels of Figure 5.3 are summarized in Figure 5.4 where the annual numbers of HSS/CIR (blue curve) and CME (red curve) flows are shown. The occurrence rate of CMEs peaks during solar maximum [*Webb*, 1991; *Yashiro et al.*, 2004; *Gopalswamy*, 2006; *Robbrecht et al.*, 2009], and storms during solar maxima tend to be CME-driven, while the HSS/CIR occurrence rate peaks during the late declining phase of the solar cycle [*Mursula and Zieger*, 1996; *Mursula et al.*, 2015], and storms in the declining phase tend to be HSS/CIR-driven [*Richardson et al.*, 2001; *Holappa et al.*, 2014]. CME-driven geomagnetic storms are brief, have denser plasma sheets, have strong ring currents, have solar energetic particle events, and can produce great auroras and dangerous geomagnetically induced currents. CIR-driven geomagnetic storms are of longer duration, have hotter plasmas and stronger spacecraft charging, and produce high fluxes of relativistic electrons [*Borovsky and Denton*, 2006]. Figure 5.4 clearly shows that overall, HSS/CIR events are more frequent than CMEs because CHs are typically long-lived large-scale structures in the solar corona, while the CME-related active regions are shorter-lived transient structures.

Figure 5.5 shows the annual correlation coefficients between daily HSS/CIR speed (V) and the equatorial coronal hole areas (A) for each year during 1973-

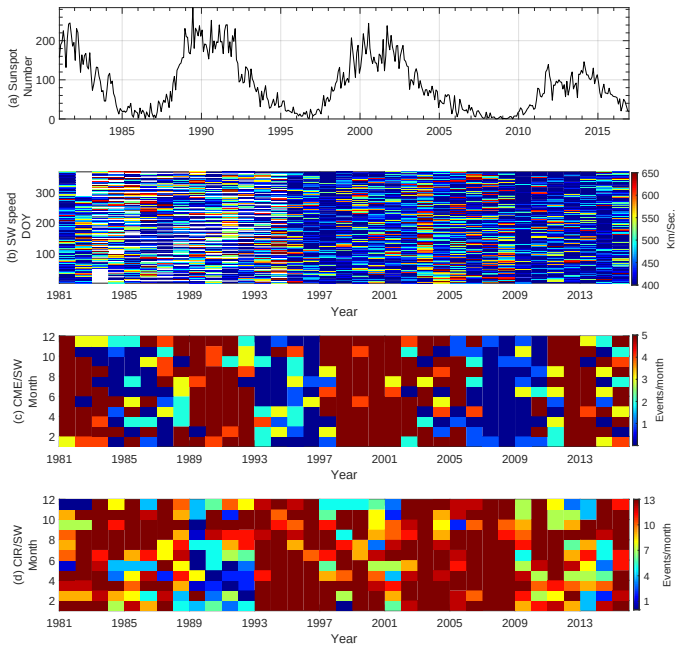

Fig. 5.3. (a) Monthly sunspot number as a reference to the solar cycles 21, 22, 23 and 24. (b) Daily solar wind speed; (c) monthly number of CME streams; and (d) HSS/CIR streams.

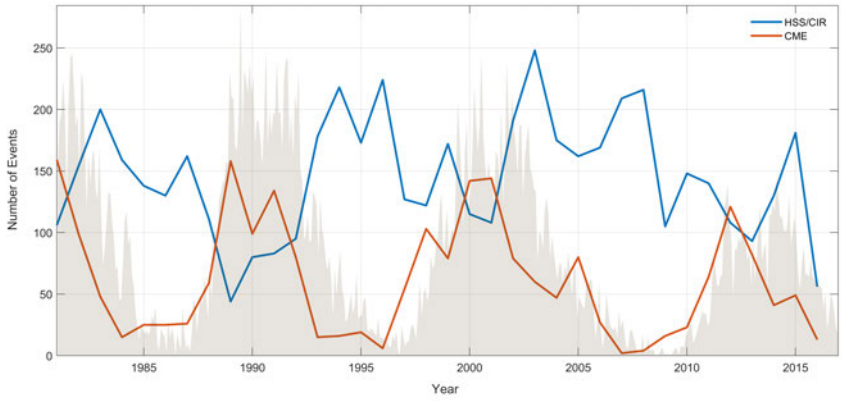

Fig. 5.4. Annual numbers of the two dominant SW flow types, HSS/CIRs (blue), and CME-associated flows (red). Monthly sunspot numbers are shaded in the background for reference.

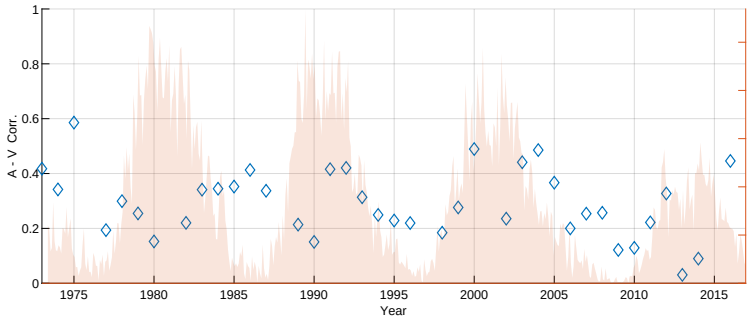

Fig. 5.5. Annual correlation coefficients between daily HSS/CIR speed (V) and the equatorial coronal hole areas (A) in 1973-2016. Sunspot numbers are plotted on the background as a reference.

2016. Maximum correlations are typically found either in the early (cycle 22), and mid-(cycle 23) or late (cycle 21) declining phase of the solar cycle. This is due to the fact that the PCH extensions and isolated equatorial CHs are more prominent at these times.

5.2. Russell-McPherron effect

The semiannual variation in geomagnetic activity has been recognized a long time ago [*Cortie*, 1912]. The maxima appear around equinoxes and the minima around solstices [*Cliver et al.*, 2000]. While also other mechanisms exist, the Russell-McPherron (R-M) effect [*Russell and McPherron*, 1973] explains the semiannual variation in geomagnetic activity with the angle (θ) between Z-axis of the geocentric solar magnetospheric (GSM) coordinate system and the Y-axis of the geocentric solar equatorial (GSEQ) coordinate system. This angle varies seasonally and diurnally (Figure 5.6) and affects the projection of IMF field lines (roughly in solar equatorial plane) to the Earth's magnetic axis (in GSM XZ-plane).

The southward component of IMF is dominantly affect the energy input from the solar wind into the magnetosphere and thus also geomagnetic activity. The Earth's rotation axis with a tilt of 23.5° from the Z-axis of the geocentric solar ecliptic (GSE) coordinate system, which causes a seasonal variation of the projection of IMF onto the GSM Z-axis and thus produce a seasonal variation of the occurrence of southward IMF in GSM. The magnetic dipole axis inclines 11.5° from the rotation axis and leads to a diurnal variation of the southward IMF projection. *Russell et al.* [2003] demonstrated that the tilt of dipole axis controls the

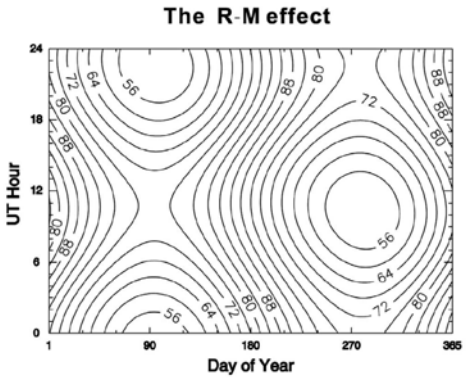

Fig. 5.6. Seasonal and diurnal variation of the angle between the GSM Z-axis and the GSEQ Y-axis [*Zhao and Zong*, 2012].

size of dayside reconnection region and thus the reconnection rate and geomagnetic activity.

We monitored the Russell-McPherron effect by studying two sequences of five HSS/CIR events, observed at 1 AU in July 2007 - August 2008 [Paper II]. These two HSS/CIR sequences had opposite magnetic polarities, and they originated from two persistent low-latitude coronal holes with corresponding polarities (Figure 5.7). We found that the sequence with negative interplanetary magnetic field polarity (toward sector) develops systematically a more negative Bz(GSM) component and becomes relatively more geoeffective when moving from winter solstice in 2007 to spring equinox in 2008 (Figure 5.8). On the other hand, the sequence with positive polarity (away sector) develops systematically a less negative Bz(GSM) component and becomes relatively less geoeffective. These changes allow the first detailed monitoring of the turning on of the Russell-McPherron effect when moving from solstice to equinox and the development of the related changes in high-latitude geomagnetic activity and geomagnetic storms.

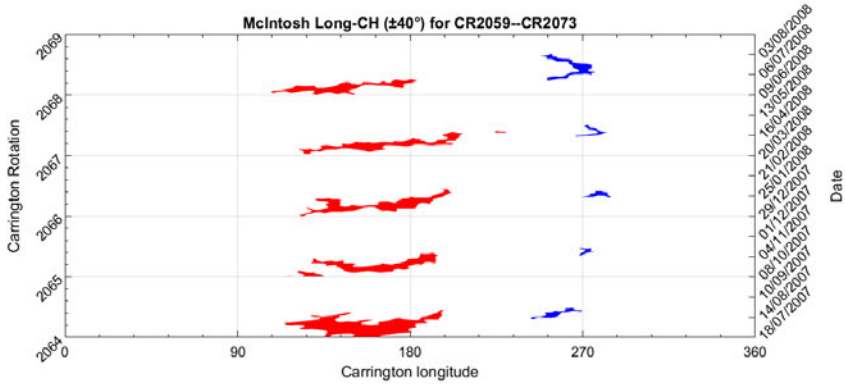

Fig. 5.7. Stack plot of equatorial slices (+40°:−40° of heliolatitude) extracted from coronal hole maps of the McIntosh Archive during July 2007-August 2008 [Paper II]. Positive polarity holes depicted in red and the negative polarity holes in blue, opposite to the ones in the original paper.

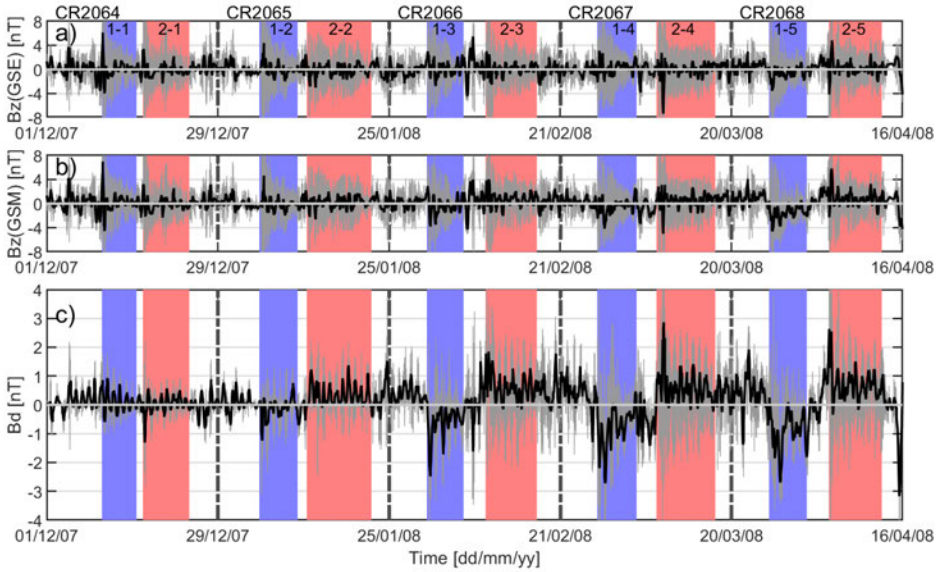

Fig. 5.8. Temporal evolution of the IMF Bz component. From top to bottom: Bz(GSE) component, Bz(GSM) component and their difference Bd = Bz(GSM) - Bz(GSE). The 1-min resolution data are depicted in grey, and the black line is its 6-hr running mean curve. HSS/CIR sequence 1 (2) is marked with red (blue) colour. Carrington rotations are marked with vertical dash-dotted bars [Paper II].

6. Summary and conclusions

As the coronal holes (CHs) are the main source for the high speed streams, their identification and tracking on the solar surface is important. It is also required for a better understanding of CH evolution during different phases of the solar cycle. It is still difficult to uniquely and objectively identify CHs on solar images as they appear differently in different wavelengths. The area, shape, and darkness of any given CH are not the same in different observing wavelengths. Different methods have been developed to identify CH boundaries manually or automatically. Coronal holes manually identified on solar synoptic maps were collected in the McIntosh Archive (McA) which consists of a hand-drawn Carrington maps based on He-I 10830Å solar observations from Kitt Peak National Observatory (KPNO). Automated CH identification attempts have used different techniques and different CH thresholds. Moreover, most studies identifying CHs consider a relatively short period of data and use a single wavelength to identify CHs.

In Paper I we presented a novel algorithm of automatically identifying CHs from EUV synoptic maps based on Solar and Heliospheric Observatory/Extreme ultraviolet Imaging Telescope (SOHO/EIT) and Solar Dynamics Observatory/Atmospheric Imaging Assembly (SDO/AIA) observations at three different wavelengths. We used all the available synoptic maps from 1996 – 2017. This algorithm uses the synoptic maps to find an optimal threshold intensity for CHs for each synoptic map separately by determining the best location and size for a segment of the synoptic map that optimally contains portions of CHs and the surrounding quiet Sun regions. Thus, the method is able to adjust itself to the changing scale size of CHs and to temporally varying (either naturally or due to changes in detector properties or intensity scaling of EUV synoptic maps) intensities. The algorithm also differentiates the filament channels from coronal holes by the relative magnetic flux imbalance. Improving the previous CH identification routines, the new algorithm provides a robust tool which facilitates long-term CH studies. In Paper I, we found considerable differences between SOHO/EIT and SDO/AIA synoptic maps, which result from instrument degradation and various other data processing issues. These differences have been further studied in Paper III.

In Paper II we studied two series of HSSs generated by two persistent low-latitude CHs that repeated almost unchanged during five solar rotations CR2064–CR2068 (December 2007–April 2008). The two HSSs had oppositely oriented IMF polarities. Each HSS/CIR event triggered a geomagnetic storm and strong high-latitude activity. We followed the evolution of the properties and geomagnetic effects of the two HSS/CIR sequences and found that the sequence with negative interplanetary magnetic field polarity (toward sector) develops systematically a more negative Bz(GSM) component and becomes relatively more geoeffective when moving from winter solstice in 2007 to spring equinox in 2008. On the other hand, the sequence with positive polarity (away sector) develops systematically a less negative Bz(GSM) component and becomes relatively less geoeffective. These changes allow the first detailed monitoring of the turning on and turning off of the Russell-McPherron effect when moving from winter solstice to spring equinox and the development of the related changes in high-latitude geomagnetic activity and geomagnetic storms.

In Paper III we dealt with the differences in SOHO/EIT and SDO/AIA synoptic maps found in Paper I and presented a new solar EUV synoptic map dataset based on full-disk images from the SOHO/EIT and SDO/AIA. We constructed new synoptic maps for both instruments using the same spatial resolution in order to reduce the differences between the maps that may result from different image resolution or different image sampling frequency. We standardized these new synoptic maps in logarithmic intensity scale to reduce the problems due to significant and complicated drifts in the SOHO/EIT and SDO/AIA intensities. We developed a method to scale the EIT pixel values to the AIA level by determining how much the standardized EIT log-intensities should be changed so that their overall cumulative probability matches that of AIA. These maps have the same relative intensity distributions for the same EIT and AIA maps, and are well suited to study the evolution of different coronal structures such as coronal holes over solar cycle timescales, where data homogeneity is important.

In Paper IV we applied the automated CH identification algorithm on the new homogenised EUV synoptic maps and produced new CH synoptic maps for 1996–2018. These were compared and combined with CH data in McIntosh Archive. We found that, although the polar coronal holes produced by the automated algorithm suffer from the vantage point effect, there is a good match between the CH datasets at nonpolar latitudes. Accordingly, the new CH dataset can be used to extend the McA coronal hole dataset quite reliably at most latitudes for the last decade.

References

Abramenko, V., V. Yurchyshyn, and H. Watanabe, Parameters of the magnetic flux inside coronal holes, *Solar Physics*, *260*(1), 43–57, doi:10.1007/s11207-009-9433-7, 2009.

Aschwanden, M. J., P. Boerner, C. J. Schrijver, and A. Malanushenko, Automated Temperature and Emission Measure Analysis of Coronal Loops and Active Regions Observed with the Atmospheric Imaging Assembly on the Solar Dynamics Observatory (SDO/AIA), *Solar Physics*, *283*(1), 5–30, 2013.

Asikainen, T., and M. Ruopsa, Solar wind drivers of energetic electron precipitation, *Journal of Geophysical Research: Space Physics*, *121*(3), 2209–2225, doi:10.1002/2015JA022215, 2016.

Babcock, The Topology of the Sun's Magnetic Field and the 22-YEAR Cycle., *The Astrophysical Journal*, *133*, 572, doi:10.1086/147060, 1961.

Babcock, H. D., The Sun's Polar Magnetic Field., *The Astrophysical Journal*, *130*, 364, doi:10.1086/146726, 1959.

Bagashvili, S., et al., Statistical properties of coronal hole rotation rates: Are they linked to the solar interior?, *Astronomy and Astrophysics*, *603*, 1–8, doi:10.1051/0004-6361/201630377, 2017.

Bame, S. J., J. R. Asbridge, W. C. Feldman, and J. T. Gosling, Solar cycle evolution of high-speed solar wind streams, *The Astrophysical Journal*, *207*, 977, doi:10.1086/154566, 1976.

Barra, V., V. Delouille, M. Kretzschmar, and J.-F. Hochedez, Fast and robust segmentation of solar EUV images: algorithm and results for solar cycle 23, *Astronomy and Astrophysics*, *505*(1), 361–371, doi:10.1051/0004-6361/200811416, 2009.

Belcher, J. W., and L. Davis, Large-amplitude Alfvén waves in the interplanetary medium, 2, *Journal of Geophysical Research*, *76*(16), 3534–3563, doi:10.1029/JA076i016p03534, 1971.

Benevolenskaya, E. E., A. G. Kosovichev, and P. H. Scherrer, Detection of high-latitude waves of solar coronal activity in extreme-ultraviolet data from the Solar and Heliospheric Observatory EUV Imaging Telescope, *The Astrophysical Journal*, *554*, L107–L110, doi:10.1086/320925, 2001.

Benz, A. O., Flare observations, *Living Reviews in Solar Physics*, *5*(1), 1, doi:10.12942/lrsp-2008-1, 2008.

Biermann, L., Kometenschweife und solare korpuskularstrahlung, *Zeit. Astrophys.*, *29*, 274–286, 1951.

Bilenko, I. A., Coronal holes and the solar polar field reversal, *Astronomy & Astrophysics*, *396*(2), 657–666, doi:10.1051/0004-6361:20021412, 2002.

Bilenko, I. A., and K. S. Tavastsherna, Coronal hole and solar global magnetic field evolution in 1976 –2012, *Solar Physics*, *291*(8), 2329–2352, doi:10.1007/s11207-016-0966-2, 2016.

Borovsky, J. E., and M. H. Denton, Differences between CME-driven storms and CIR-driven storms, *Journal of Geophysical Research*, *111*(A7), A07S08, doi:10.1029/2005JA011447, 2006.

Borovsky, J. E., and M. H. Denton, The differences between storms driven by helmet streamer CIRs and storms driven by pseudostreamer CIRs, *Journal of Geophysical Research: Space Physics*, *118*(9), 5506–5521, doi:10.1002/jgra.50524, 2013.

Bravo, S., and G. A. Stewart, The correlation between sunspot and coronal hole cycles and a forecast of the maximum of sunspot cycle 23, *Solar Physics*, *173*(1), 193–198, doi:10.1023/A:1004916427722, 1996.

Bumba, V., M. Klvana, and J. Sykora, Coronal holes and their relation to the background and local magnetic fields., *aap*, *298*, 923, 1995.

Charbonneau, P., Dynamo models of the solar cycle, *Living Reviews in Solar Physics*, *7*(1), 3, doi:10.12942/lrsp-2010-3, 2010.

Cliver, E. W., Y. Kamide, and A. G. Ling, Mountains versus valleys: Semiannual variation of geomagnetic activity, *Journal of Geophysical Research: Space Physics*, *105*(A2), 2413–2424, doi:10.1029/1999JA900439, 2000.

Cortie, A. L., Sunspot and terrestrial magnetic phenomena, 1898-1911, *Mon. Not. R. Astron. Soc.*, *73*, 52–60, 1912.

Cranmer, S. R., Coronal holes, *Living Reviews in Solar Physics*, *6*(3), 2009.

Cranmer, S. R., and A. A. van Ballegooijen, On the Generation, Propagation, and Reflection of Alfven Waves from the Solar Photosphere to the Distant Heliosphere, *The Astrophysical Journal Supplement Series*, *156*(2), 265–293, doi:10.1086/426507, 2005.

de Toma, G., Evolution of coronal holes and implications forâ high-speed solar wind during the minimum between cycles 23 and 24, *Solar Physics*, *274*(1), 195–217, doi:10.1007/s11207-010-9677-2, 2011.

Delaboudinière, J. P., et al., EIT: Extreme-ultraviolet Imaging Telescope for the SOHO mission, *Solar Physics*, *162*(1-2), 291–312, doi:10.1007/BF00733432, 1995.

Dikpati, M., and P. A. Gilman, Flux-transport solar dynamos, *Space Science Reviews*, *144*(1-4), 67–75, doi:10.1007/s11214-008-9484-3, 2009.

Dowdy, J. F., D. Rabin, and R. L. Moore, On the magnetic structure of the quiet transition region, *Solar Physics*, *105*(1), 35–45, doi:10.1007/BF00156374, 1986.

Echer, E., B. T. Tsurutani, and W. D. Gonzalez, Interplanetary origins of moderate (-100 nT $<$ Dst $\leq$ -50 nT) geomagnetic storms during solar cycle 23 (1996-2008), *J. Geophys. Res.*, *118*, 385–392, doi:10.1029/2012JA018086, 2013.

Gabriel, A. H., A Magnetic Model of the Solar Transition Region, *Philosophical Transactions of the Royal Society of London Series A*, *281*(1304), 339–352, doi:10.1098/rsta.1976.0031, 1976.

Geiss, J., et al., The southern high-speed stream: results from the SWICS instrument on Ulysses, *Science*, *268*(5213), 1033–1036, doi:10.1126/SCIENCE.7754380, 1995.

Georgobiani, D., A. G. Kosovichev, R. Nigam, Å. Nordlund, and R. F. Stein, Numerical Simulations of Oscillation Modes of the Solar Convection Zone, *The Astrophysical Journal*, *530*(2), L139–L142, doi:10.1086/312490, 2000.

Gibson, S. E., and B. C. Low, A time-dependent three-dimensional magnetohydrodynamic model of the coronal mass ejection, *The Astrophysical Journal*, *493*(1), 460–473, doi:10.1086/305107, 1998.

Gibson, S. E., D. Webb, I. M. Hewins, R. H. McFadden, B. A. Emery, and W. Denig, Beyond sunspots: Studies using the McIntosh Archive of global solar magnetic field patterns, *Proceedings of the International Astronomical Union*, *12*(328), 93–100, doi:10.1017/S1743921317003726, 2016.

Golubeva, E. M., and A. V. Mordvinov, Rearrangements of open magnetic flux and formation of polar coronal holes in cycle 24, *Solar Physics*, *292*(11), 175, doi:10.1007/s11207-017-1200-6, 2017.

Gopalswamy, N., Coronal mass ejections of solar cycle 23, *Journal of Astrophysics and Astronomy*, *27*(2), 243–254, doi:10.1007/BF02702527, 2006.

Gosling, J. T., D. J. McComas, J. L. Phillips, and S. J. Bame, Geomagnetic activity associated with earth passage of interplanetary shock disturbances and coronal mass ejections, *Journal of Geophysical Research*, *96*(A5), 7831, doi:10.1029/91JA00316, 1991.

Gringauz, K. I., V. V. Bezrokikh, V. D. Ozerov, and R. E. Rybchinskii, A Study of the Interplanetary Ionized Gas, High-Energy Electrons and Corpuscular Radiation from the Sun by Means of the Three-Electrode Trap for Charged Particles on the Second Soviet Cosmic Rocket, *Soviet Physics Doklady*, *5*, 361, 1960.

Hale, G. E., On the Probable Existence of a Magnetic Field in Sun-Spots, *The Astrophysical Journal*, *28*, 315, doi:10.1086/141602, 1908.

Hamada, A., T. Asikainen, I. Virtanen, and K. Mursula, Automated Identification of Coronal Holes from Synoptic EUV Maps, *Solar Physics*, *293*(4), doi:10.1007/s11207-018-1289-2, 2018.

Harvey, J., and J. Worden, New Types and Uses of Synoptic Maps, in *Synoptic Solar Physics*, *Astronomical Society of the Pacific Conference Series*, vol. 140, edited by K. S. Balasubramaniam, J. Harvey, and D. Rabin, p. 155, 1998.

Harvey, K. L., and F. Recely, Polar Coronal Holes During Cycles 22 and 23, *Solar Physics*, *211*(1/2), 31–52, doi:10.1023/A:1022469023581, 2002.

Hess Webber, S. A., N. Karna, W. D. Pesnell, and M. S. Kirk, Areas of polar coronal holes from 1996 through 2010, *Solar Physics*, *289*(11), 4047–4067, doi:10.1007/s11207-014-0564-0, 2014.

Hoeksema, J. T., et al., The Helioseismic and Magnetic Imager (HMI) Vector Magnetic Field Pipeline: Overview and Performance, *Solar Physics*, *289*(9), 3483–3530, doi:10.1007/s11207-014-0516-8, 2014.

Hofmeister, S. J., A. Veronig, M. A. Reiss, M. Temmer, S. Vennerstrom, B. Vršnak, and B. Heber, Characteristics of Low-latitude Coronal Holes near the Maximum of Solar Cycle 24, *The Astrophysical Journal*, *835*(2), 268, doi:10.3847/1538-4357/835/2/268, 2017.

Holappa, L., K. Mursula, T. Asikainen, and I. G. Richardson, Annual fractions of high-speed streams from principal component analysis of local geomagnetic activity, *J. Geophys. Res.*, *119*(6), 4544–4555, doi:10.1002/2014JA019958, 2014.

Howe, R., Solar Interior Rotation and its Variation, *Living Reviews in Solar Physics*, *6*(1), 1, doi:10.12942/lrsp-2009-1, 2009.

Hudson, H. S., Global Properties of Solar Flares, *Space Science Reviews*, *158*(1), 5–41, doi:10.1007/s11214-010-9721-4, 2011.

Hundhausen, A. J., An interplanetary view of coronal holes., *Coronal holes and high speed wind streams, p. 225 - 329*, pp. 225–329, 1977.

Huttunen, K. E. J., H. E. J. Koskinen, and R. Schwenn, Variability of magnetospheric storms driven by different solar wind perturbations, *Journal of Geophysical Research*, *107*(A7), 1121, doi:10.1029/2001JA900171, 2002.

Illarionov, E. A., and A. G. Tlatov, Segmentation of coronal holes in solar disc images with a convolutional neural network, *Monthly Notices of the Royal Astronomical Society*, *481*(4), 5014–5021, doi:10.1093/mnras/sty2628, 2018.

Inglis, A. R., R. E. O'Connor, W. D. Pesnell, M. S. Kirk, and N. Karna, Characteristics of ephemeral coronal holes, *The Astrophysical Journal*, *880*(2), 98, doi:10.3847/1538-4357/ab27c1, 2019.

Kahler, S. W., and H. S. Hudson, Boundary Structures and Changes in Long lived Coronal Holes, *The Astrophysical Journal*, *574*(1), 467–476, doi:10.1086/340937, 2002.

Kahler, S. W., J. M. Davis, and J. W. Harvey, Comparison of coronal holes observed in soft X-ray and He 10830 Å spectroheliograms, *Sol. Phys.*, *87*, 47, 1983.

Karna, N., S. A. Hess Webber, and W. D. Pesnell, Using Polar Coronal Hole Area Measurements to Determine the Solar Polar Magnetic Field Reversal in Solar Cycle 24, *Solar Physics*, *289*(9), 3381–3390, doi:10.1007/s11207-014-0541-7, 2014.

Karna, N., J. Zhang, W. D. Pesnell, and S. A. H. Webber, Study of the 3d geomagnetic structure and temperature of a coronal cavity using the limb synoptic map method, *The Astrophysical Journal*, *810*(2), 124, doi:10.1088/0004-637X/810/2/124, 2015.

Kilpua, E. K. J., A. Balogh, R. von Steiger, and Y. D. Liu, Geoeffective Properties of Solar Transients and Stream Interaction Regions, *Space Science Reviews*, *212*(3-4), 1271–1314, doi:10.1007/s11214-017-0411-3, 2017.

Kirk, M. S., W. D. Pesnell, C. A. Young, and S. A. Hess Webber, Automated detection of EUV Polar Coronal Holes during Solar Cycle 23, *Sol. Phys.*, *257*, 99–112, doi:10.1007/s11207-009-9369-y, 2009.

Klimchuk, J. A., Nanoflare Heating: Observations and Theory, *arXiv e-prints*, arXiv:1709.07320, 2017.

Krieger, A. S., A. F. Timothy, and E. C. Roelof, A coronal hole and its identification as the source of a high velocity solar wind stream, *Sol. Phys.*, *29*, 505–525, 1973.

Krista, L. D., and P. T. Gallagher, Automated coronal hole detection using local intensity thresholding techniques, *Solar Physics*, *256*(1), 87–100, doi:10.1007/s11207-009-9357-2, 2009.

Lang, K. R., *The Cambridge encyclopedia of the sun*, 256 pp., Cambridge University Press, 2001.

Leighton, R. B., A Magneto-Kinematic Model of the Solar Cycle, *The Astrophysical Journal*, *156*, 1, doi:10.1086/149943, 1969.

Lemen, J. R., et al., The Atmospheric Imaging Assembly (AIA) on the Solar Dynamics Observatory (SDO), *Solar Physics*, *275*(1-2), 17–40, doi:10.1007/s11207-011-9776-8, 2011.

Livingston, W., J. W. Harvey, O. V. Malanushenko, and L. Webster, Sunspots with the Strongest Magnetic Fields, *Solar Physics*, *239*(1-2), 41–68, doi:10.1007/s11207-006-0265-4, 2006.

Lowder, C., Q. Jiong, and R. Leamon, Coronal holes and open magnetic flux over cycles 23 and 24, *Solar Physics*, *292*(1), 18, doi:10.1007/s11207-016-1041-8, 2017.

Luhmann, J. G., Y. Li, C. N. Arge, P. R. Gazis, and R. Ulrich, Solar cycle changes in coronal holes and space weather cycles, *J. Geophys. Res.*, *107(A8)*, 1154, doi:10.1029/2001JA007550, 2002.

Manoharan, P. K., Three-dimensional evolution of solar wind during solar cycles 22-24, *The Astrophysical Journal*, *751*(2), 128, doi:10.1088/0004-637x/751/2/128, 2012.

McComas, D. J., H. A. Elliott, N. A. Schwadron, J. T. Gosling, R. M. Skoug, and B. E. Goldstein, The three-dimensional solar wind around solar maximum, *Geophysical Research Letters*, *30*(10), n/a–n/a, doi:10.1029/2003GL017136, 2003.

McComas, D. J., et al., Solar wind observations over Ulysses' first full polar orbit, *Journal of Geophysical Research: Space Physics*, *105*(A5), 10,419–10,433, doi:10.1029/1999JA000383, 2000.

McIntosh, P. S., R. J. Thompson, and E. C. Willock, A 600-day periodicity in solar coronal holes, *Nature*, *360*, 322–324, 1992.

Mursula, K., and B. Zieger, The 13.5-day periodicity in the Sun, solar wind, and geomagnetic activity: The last three solar cycles, *Journal of Geophysical Research: Space Physics*, *101*(A12), 27,077–27,090, doi:10.1029/96JA02470, 1996.

Mursula, K., R. Lukianova, and L. Holappa, Occurrence of high-speed solar wind streams over the grand modern maximum, *The Astrophysical Journal*, *801*(1), 30, doi:10.1088/0004-637X/801/1/30, 2015.

Narain, U., and P. Ulmschneider, Chromospheric and coronal heating mechanisms II, *Space Science Reviews*, *75*(3-4), 453–509, doi:10.1007/BF00833341, 1996.

Nolte, J. T., A. S. Krieger, A. F. Timothy, R. E. Gold, E. C. Roelof, G. Vaiana, A. J. Lazarus, J. D. Sullivan, and P. S. McIntosh, Coronal holes as sources of solar wind, *Solar Physics*, *46*(2), 303–322, doi:10.1007/BF00149859, 1976.

Okamoto, T. J., and T. Sakurai, Super-strong Magnetic Field in Sunspots, *The Astrophysical Journal Letters*, *852*(1), L16, doi:10.3847/2041-8213/AAA3D8, 2018.

Parker, E. N., Dynamics of the interplanetary gas and magnetic fields, *Astrophys. J.*, *128*, 664–676, 1958.

Pesnell, W. D., B. J. Thompson, and P. C. Chamberlin, The Solar Dynamics Observatory (SDO), *Solar Physics*, *275*(1-2), 3–15, doi:10.1007/s11207-011-9841-3, 2012.

Phillips, K. J. H., *Guide to the Sun*, vol. 1846, 41 pp., Cambridge University Press, 1992.

Pizzo, V., A three-dimensional model of corotating streams in the solar wind, 1. Theoretical foundations, *Journal of Geophysical Research*, *83*(A12), 5563, doi:10.1029/ja083ia12p05563, 1978.

Podladchikova, O., T. D. de Wit, V. Krasnoselskikh, and B. Lefebvre, Quiet Sun coronal heating: analyzing large scale magnetic structures driven by different small-scale uniform sources, *Astronomy and Astrophysics, v.382, p.713-721 (2002)*, *382*, 713–721, doi:10.1051/0004-6361:20011637, 2002.

Reiss, M. A., S. J. Hofmeister, R. De Visscher, M. Temmer, A. M. Veronig, V. Delouille, B. Mampaey, and H. Ahammer, Improvements on coronal hole detection in SDO/AIA images using supervised classification, *Journal of Space Weather and Space Climate*, *5*, A23, doi:10.1051/swsc/2015025, 2015.

Richardson, I. G., and H. V. Cane, Solar wind drivers of geomagnetic storms during more than four solar cycles, *Journal of Space Weather and Space Climate*, *2*, A01, doi:10.1051/swsc/2012001, 2012.

Richardson, I. G., E. W. Cliver, and H. V. Cane, Sources of geomagnetic storms for solar minimum and maximum conditions during 1972-2000, *Geophys. Res. Lett.*, *28*, 2569–2572, 2001.

Rieutord, M., and F. Rincon, The Sun's Supergranulation, *Living Reviews in Solar Physics*, *7*(1), 2, doi:10.12942/lrsp-2010-2, 2010.

Robbrecht, E., D. Berghmans, R. A. M. Van der Linden, E. Robbrecht, D. Berghmans, and R. A. M. Van der Linden, Automated LASCO CME catalog for solar cycle 23: are CMEs scale invariant?, *The Astrophysical Journal*, *691*(2), 1222–1234, doi:10.12942/lrsp-2010-1., 2009.

Russell, C. T., and R. L. McPherron, Semiannual variation of geomagnetic activity, *Journal of Geophysical Research*, *78*(1), 92–108, doi:10.1029/JA078i001p00092, 1973.

Russell, C. T., Y. L. Wang, and J. Raeder, Possible dipole tilt dependence of dayside magnetopause reconnection, *Geophysical Research Letters*, *30*(18), doi:10.1029/2003GL017725, 2003.

Sánchez Almeida, J., J. A. Bonet, B. Viticchié, and D. D. Moro, MAGNETIC BRIGHT POINTS IN THE QUIET SUN, *The Astrophysical Journal*, *715*(1), L26–L29, doi:10.1088/2041-8205/715/1/L26, 2010.

Scherrer, P. H., et al., The Solar Oscillations Investigation - Michelson Doppler Imager, *Solar Physics*, *162*(1-2), 129–188, doi:10.1007/BF00733429, 1995.

Scholl, I. F., and S. R. Habbal, Automatic detection and classification of coronal holes and filaments based on euv and magnetogram observations of the solar disk, *Solar Physics*, *248*(2), 425–439, doi:10.1007/s11207-007-9075-6, 2008.

Schou, J., et al., Helioseismic Studies of Differential Rotation in the Solar Envelope by the Solar Oscillations Investigation Using the Michelson Doppler Imager, *The Astrophysical Journal*, *505*(1), 390–417, doi:10.1086/306146, 1998.

Schou, J., et al., Design and Ground Calibration of the Helioseismic and Magnetic Imager (HMI) Instrument on the Solar Dynamics Observatory (SDO), *Solar Physics*, *275*(1-2), 229–259, doi:10.1007/s11207-011-9842-2, 2012.

Schwabe, H., Sonnen — Beobachtungen im Jahre 1843, *Astronomische Nachrichten*, *21*(15), 234–235, doi:10.1002/asna.18440211505, 1844.

Sibeck, D. G., and J. D. Richardson, Toward forecasting space weather in the heliosphere, *Journal of Geophysical Research: Space Physics*, *102*(A7), 14,721–14,733, doi:10.1029/97JA01119, 1997.

Snodgrass, H. B., and R. K. Ulrich, Rotation of Doppler features in the solar photosphere, *The Astrophysical Journal*, *351*, 309, doi:10.1086/168467, 1990.

Snyder, C. W., M. Neugebauer, and U. R. Rao, The solar wind velocity and its correlation with cosmic ray variations and solar and geomagnetic activity, *J. Geophys. Res.*, *68*, 6361–6370, 1963.

Sojka, J. J., R. L. McPherron, A. P. van Eyken, M. J. Nicolls, C. J. Heinselman, and J. D. Kelly, Observations of ionospheric heating during the passage of solar coronal hole fast streams, *Geophysical Research Letters*, *36*(19), L19,105, doi:10.1029/2009GL039064, 2009.

Svalgaard, L., T. L. Duvall, and P. H. Scherrer, The strength of the Sun's polar fields, *Solar Physics*, *58*(2), 225–239, doi:10.1007/BF00157268, 1978.

Thompson, B. J., S. P. Plunkett, J. B. Gurman, J. S. Newmark, O. C. St. Cyr, and D. J. Michels, Soho/eit observations of an earth-directed coronal mass ejection on may 12, 1997, *Geophysical Research Letters*, *25*(14), 2465–2468, doi:10.1029/98GL50429, 1998.

Timothy, A. F., A. S. Krieger, and G. S. Vaiana, The structure and evolution of coronal holes, *Solar Physics*, *42*(1), 135–156, doi:10.1007/BF00153291, 1975.

Tousey, R., G. D. Sandlin, and J. D. Purcell, On Some Aspects of XUV Spectroheliograms, *Structure and Development of Solar Active Regions. Symposium no. 35 held in Budapest, Hungary, 4-8 September 1967. Edited by Karl Otto Kiepenheuer. International Astronomical Union. Symposium no. 35, Dordrecht, D. Reidel., p.411*, *35*, 411, 1968.

Tsuneta, S., et al., The Magnetic Landscape of the Sun's Polar Region, *The Astrophysical Journal*, *688*(2), 1374–1381, doi:10.1086/592226, 2008.

Tsurutani, B. T., W. D. Gonzalez, A. L. C. Gonzalez, F. Tang, J. K. Arballo, and M. Okada, Interplanetary origin of geomagnetic activity in the declining phase of the solar cycle, *Journal of Geophysical Research: Space Physics*, *100*(A11), 21,717–21,733, doi:10.1029/95JA01476, 1995.

Tsurutani, B. T., et al., Corotating solar wind streams and recurrent geomagnetic activity: A review, *Journal of Geophysical Research*, *111*(A7), A07S01, doi:10.1029/2005JA011273, 2006.

Verbanac, G., B. Vršnak, A. Veronig, and M. Temmer, Equatorial coronal holes, solar wind high-speed streams, and their geoeffectiveness, *Astronomy & Astrophysics*, *526*, A20, doi:10.1051/0004-6361/201014617, 2011.

Verbeeck, C., Delouille, V., Mampaey, B., and De Visscher, R., The spoca-suite: Software for extraction, characterization, and tracking of active regions and coronal holes on euv images, *A&A*, *561*, A29, doi:10.1051/0004-6361/201321243, 2014.

Virtanen, I., and K. Mursula, Photospheric and coronal magnetic fields in six magnetographs I . Consistent evolution of the bashful ballerina, *Astronomy & Astrophysics*, *16*(28096), 1–10, 2016.

Vršnak, B., M. Temmer, and A. M. Veronig, Coronal Holes and Solar Wind High-Speed Streams: I. Forecasting the Solar Wind Parameters, *Solar Physics*, *240*(2), 315–330, doi:10.1007/s11207-007-0285-8, 2007.

Waldmeier, M., *Die Sonnenkorona*, vol. II, Verlag Birkhäuser, Basel, Switzerland, 1957.

Waldmeier, M., Cyclic variation of the polar coronal hole, *Sol. Phys.*, *70*, 251–258, 1981.

Wang, Y.-M., The sun's large-scale magnetic field and its long-term evolution, *Solar Physics*, *224*(1), 21–35, doi:10.1007/s11207-005-4982-x, 2004.

Wang, Y.-M., S. H. Hawley, and N. R. Sheeley, Jr., The magnetic nature of coronal holes, *Science*, *271*, 464–469, doi:10.1126/science.271.5248.464, 1996.

Webb, D. F., The solar cycle variation of the rates of CMEs and related activity, *Advances in Space Research*, *11*(1), 37–40, doi:10.1016/0273-1177(91)90086-Y, 1991.

Wilhelm, K., I. E. Dammasch, E. Marsch, and D. M. Hassler, On the source regions of the fast solar wind in polar coronal holes, *Astron. Astrophys*, *353*, 749–756, 2000.

Woch, J., W. I. Axford, U. Mall, B. Wilken, S. Livi, J. Geiss, G. Gloeckler, and R. J. Forsyth, SWICS/Ulysses observations: The three-dimensional structure of the heliosphere in the declining/minimum phase of the solar cycle, *Geophysical Research Letters*, *24*(22), 2885–2888, doi:10.1029/97GL01605, 1997.

Yashiro, S., N. Gopalswamy, G. Michalek, O. C. St. Cyr, S. P. Plunkett, N. B. Rich, and R. A. Howard, A catalog of white light coronal mass ejections observed by the soho spacecraft, *J. Geophys. Res.*, *109*, A07105, 2004.

Zhang, J., et al., Solar and interplanetary sources of major geomagnetic storms (Dst $\leq$ -100 nT) during 1996-2005, *J. Geophys. Res.*, *112*(A11), A10,102, doi:10.1029/2007JA012321, 2007.

Zhao, H., and Q. Zong, Seasonal and diurnal variation of geomagnetic activity: Russell-McPherron effect during different IMF polarity and/or extreme solar wind conditions, *Journal of Geophysical Research: Space Physics*, *117*(A11), doi:10.1029/2012JA017845, 2012.

Zirker, J. B., Coronal holes and high speed wind streams: a monograph from Skylab solar workshop I., *Coronal holes and high speed wind streams: a monograph from Skylab solar workshop I., by Zirker, J. B.. Boulder, CO (USA): Colorado Associated University Press, 454 p.*, 1977.